Radio Astronomy, Planetary

Samuel Gulkis, Jet Propulsion Laboratory, California Institute of Technology
Imke de Pater, University of California, Berkeley

Glossary

Antenna temperature: Measure of the noise power collected by the antenna and delivered to the radio receiver. Specifically, the temperature at which a resistor, substituted for the antenna, would have to be maintained in order to deliver the same noise power to the receiver in the same frequency bandwidth.

Blackbody: Idealized object that absorbs all electromagnetic radiation that is incident on it. The radiation properties of blackbody radiators are described by the Planck function. Planetary radio astronomers use the properties of blackbody radiators to describe the radiation from planets.

Brightness temperature: The definition is not unique; great care is needed to decipher the intentions of the authors. The temperature at which a blackbody radiator would radiate an intensity of electromagnetic radiation identical to that of the planet for a specific frequency, frequency bandwidth, and polarization under consideration is one definition of brightness temperature. A second definition is that it is the intensity of radiation under consideration divided(normalized) by the factor ($\lambda^2/2k$). The normalization factor dimensionally scales the intensity to have units of temperature. The two definitions show the largest departures at low temperatures and high frequencies.

Effective area: Equivalent cross section or collecting area of a radio telescope to an incident radio wave; a measure of a radio telescope's capability to detect weak radio signals.

Effective temperature: Temperature at which a blackbody radiator would radiate over all frequencies an intensity of electromagnetic radiation identical to that radiated from a planet.

Equivalent blackbody disk temperature: Temperature of a blackbody radiator with the same solid angle as the planet that gives the same radiation intensity at the Earth as observed from the planet at a specified frequency and bandwidth.

Flux density: Power per unit area and per unit frequency of an electromagnetic wave crossing an imaginary plane surface from one side to the other. In observational radio astronomy, the mks system of units is generally used, and the units of flux density are watts per square meter per hertz.

Flux unit or jansky: Commonly used unit of flux density equal to 1×10^{-26} W m^{-2} Hz^{-1}. The size of the unit is suited to planetary radio emissions, which are very weak.

Nonthermal radio emission: Radio emission produced by processes other than thermal emission. Cyclotron and synchrotron radio emission are two examples of nonthermal radio emission.

Optical Depth: Atmospheric attenuation is usually expressed by giving the dimensionless quantity "optical depth" along a specified path. A signal that passes through an atmosphere whose optical depth is τ is attenuated by the factor $e^{-\tau}$.

Thermal radio emission: Continuous radio emission from an object that results from the object's temperature. Blackbody radiation is a form of thermal radio emission.

Planetary radio astronomy is the study of the physical characteristics of the planets in the Solar System by means of the electromagnetic radio radiation emitted by these objects. The term is also used more generally to include the study of planetary ring systems, the moon, asteroids, satellites, and comets in the Solar System. Radio astronomy generally refers to the (vacuum) wavelength range from about 0.5 mm (600 GHz = 600×10^9 Hz) to a kilometer (300 kHz) and longward. There is no wide acceptance of the upper limit frequency. Observations from the ground cannot be carried out below a few megahertz because of the Earth's ionosphere that is opaque to very low frequency radio waves. At millimeter and submillimeter wavelengths, the terrestrial atmosphere defines windows where radio emissions from cosmic sources can reach the ground. Radio emissions have been measured from all of the planets and some satellites, asteroids, and comets. The observed continuum emissions from the planets can be broadly classified as quasi-thermal (having the same general shape as a blackbody emitter) and nonthermal (i.e., cyclotron, synchrotron). Narrow spectral lines from molecules have been observed in the atmospheres of planets, satellites, and comets. Planetary radio emissions originate in the solid mantles, atmospheres, and magnetospheres of the planets. A number of Solar System spacecraft have carried radio astronomical instrumentation.

I. INTRODUCTION

A. Brief History

The science of radio astronomy began with the pioneering work of Karl G. Jansky, who discovered radio emission from the Milky Way galaxy while studying the direction of arrival of radio bursts associated with thunderstorms. Ten years later, in 1942, while trying to track down the source of radio interference on a military antiaircraft radar system in England, J.S. Hey established the occurrence of radio emission from the sun.

R.H. Dicke and R. Beringer working in the United States made the first intentional measurement of a Solar System object in 1945. They observed radio emission from the moon at a wavelength of 1.25 cm, thus beginning the first scientific studies at radio wavelengths of the planets and satellites of the Solar System. Subsequent observations revealed that the microwave emission from the moon varies with lunar phase but the amplitude of these variations is much smaller than that observed at infrared wavelengths. This result was interpreted in terms of emission originating below the surface of the moon, where the temperature variations are smaller than at the surface. Within a few years, it was widely recognized that the long wavelengths provided by radio measurements offered a new and important tool for Solar System studies, namely the capability of probing into and beneath cloud layers and surfaces of the planets. However, thermal radio emissions from the planets are exceedingly weak and nearly a decade elapsed before system sensitivity was sufficiently improved to enable the detection of planetary thermal emission.

Meanwhile, another unanticipated discovery was made. In June 1954, when the angular separation between the sun and a supernova remnant known as the Crab Nebula was small, astronomers B. Burke and K. Franklin of the Carnegie Institution were attempting to study the effect of the solar corona on radio waves from the Crab Nebula. Occasionally, they observed bursts of radio interference, which they initially thought were due to the sun. That hypothesis was discarded when it was discovered that the origin of the interference bursts was nearly fixed with respect to the background stars. Further observations and examinations of the data revealed that the emissions were in fact originating from Jupiter, which happened to be located in the same region of the sky as the sun and the Crab Nebula. Because the intensity of the emissions was much too strong to be of thermal origin, Franklin and Burke concluded that Jupiter was a source of nonthermal radio emission.

The first successful measurements of thermal emission from the planets were made in 1956 at the Naval Research Laboratory in Washington, D.C. C.H. Mayer, T.P. McCullough, and R.M. Sloanaker scanned Venus, Mars, and Jupiter with a 15-m parabolic antenna equipped with a new 3-cm wavelength radio receiver. They detected weak thermal emission from these three planets when each was observed at its closest distance to the Earth.

In the intervening years, thermal emission has been measured from all of the planets in the Solar System. Because of the faintness of its radio emission, Pluto was the last planet to be

detected. A few asteroids, satellites, and comets have been measured as well. Nonthermal radio emission has been measured from Jupiter, Saturn, Uranus, Neptune, and Earth. In this article we give an overview of the techniques used by planetary radio astronomers and discuss what has been learned from the measurements and what can be done in the future. In the interest of brevity, we do not discuss specific observations of asteroids and satellites, although they rightfully belong in any discussion of planetary radio astronomy.

B. Measurement Objectives

The primary objective of planetary exploration is to determine the physical characteristics of the planets, satellites, asteroids, and comets in order to obtain an understanding of the origin and evolution of the Solar System, including the origin of life on the planet Earth. One objective associated with this goal is to determine the composition and physical characteristics of these bodies and their atmospheres. Studies of the energy budget and redistribution of energy within solid surfaces and atmospheres are part of this work. Another objective is to investigate the magnetic fields and ionized plasmas that surround some of the bodies in the Solar System and to understand the interaction of the magnetic fields with the solar wind and the cosmic environment.

Planetary research involves many scientific disciplines and requires a variety of instruments and techniques, including astronomical studies from the Earth, planetary spacecraft flybys, orbiters, and probes, and eventually manned landings. Each of the various approaches used has a particular strength that the experimenters try to exploit. Thus far, most planetary radio astronomy has been carried out from the ground, but the techniques carry over to spacecraft as well.

Planetary radio astronomy measurements provide complementary data to other observational techniques. They also provide some unique data. For example, radio measurements can be used to provide information about planetary atmospheres and planetary subsurface materials to much greater depth than other remote sensing techniques. The greater penetration is a result of neutral gases and solids being more transparent to radio waves than higher-frequency waves such as infrared or visible light. Also, the scattering from particulate materials in planetary atmospheres is generally less at radio wavelengths than at shorter wavelengths. The relative transparency of atmospheres, clouds, and surfaces to radio waves allows the planetary radio astronomer to measure thermal profiles of planetary atmospheres beneath the cloud layers in the atmosphere and to measure temperatures beneath the solid surface of the planet. Taking advantage of this property, radio astronomers were the first to measure the very high surface temperature of cloud-covered Venus.

Very high resolution spectroscopy is another area in which radio astronomy provides a unique capability. It is possible to achieve very high spectral resolution in the radio and submillimeter spectral region by translating the frequency of the radio signal under study to a convenient place in the frequency spectrum where spectrum analysis is easier to achieve with either digital or analog techniques. This process takes place without disturbing the relation of the sidebands to the carrier frequency. The process of frequency translation is referred to by such names as heterodyne, mixing, or frequency conversion. The heterodyne technique makes it possible to measure absorption and emission line shapes in greater detail than has been possible at shorter wavelengths. Both temperature-altitude and composition-altitude profile distributions of absorbing chemical species (e.g., NH_3, H_2O, CO) can be deduced from spectroscopic measurements.

Finally, we note that both synchrotron and cyclotron radiation from (Solar System) planets is confined to the radio region of the spectrum. This circumstance is due to the range of planetary magnetic field strengths and particle energies found in the Solar System. The existence of Jupiter's strong magnetic field was first deduced from earth-based measurements of its polarized radio emission.

TABLE I. Physical Data for the Planets

	Mean distance (AU)[a]	Mass (Earth = 1)	Radius (equator) (km)	Obl.[b]	Density (g/cm^3)	Bond albedo[c]	Diameter (arc sec)[d] Min.	Max.
Mercury	0.387	0.055	2,440	Small	5.427	0.06	4.7	12.2
Venus	0.723	0.815	6,052	Small	5.204	0.77	9.9	62.2
Earth	1.000	1	6,371	1/298.2	5.515	0.39	—	—
Mars	1.524	0.107	3,390	1/156.6	3.934	0.16	3.5	24.6
Jupiter	5.203	317.9	69,911	1/16.7	1.326	0.45	30.5	49.8
Saturn	9.537	95.2	58,232	1/9.3	0.687	0.61	14.7	20.5
Uranus	19.191	14.6	25,362	1/100	1.318	0.42	3.4	4.2
Neptune	30.069	17.2	24,624	1/38.5	1.638	0.42	2.2	2.4
Pluto	39.482	0.0017	1,151	Unknown	1.1	0.55	0.06	0.1

[a] AU, Astronomical unit = 149.6×10^6 km.

[b] Obl., Oblatness of planet = 1 – (polar radius /equatorial radius).

[c] Bond Albedo, ratio of reflected solar radiation to incident solar radiation. Spectral range should be specified, for example visual Bond albedo

[d] Diameter, angular extent of disk when planet–Earth distance is greatest (min.) and least (max).

C. Physical Properties of the Planets

The physical characteristics of the planets are required in order to make qualitative estimates of the radio power flux densities expected from the planets. Table I presents physical data for the planets.

II. BASIC CONCEPTS

A. Thermal (Blackbody) Radiation

Any object in thermodynamic equilibrium with its suroundings (having a temperature above absolute zero) emits a continuous spectrum of electromagnetic radiation at all wavelengths including the radio region. This emission is referred to as thermal emission. The concept of a "blackbody" radiator is frequently used as an idealized standard which can be compared with the absorption and emission properties of real materials. A blackbody radiator is defined as an object that absorbs all electromagnetic radiation that falls on it at all frequencies over all angles of incidence. No radiation is reflected from such an object. According to thermodynamic arguments embodied in Kirchhoff's law, a good absorber is also a good emitter. The blackbody radiator emits the maximum amount of thermal radiation possible for an object at a given temperature. The radiative properties of a blackbody radiator have been well studied and verified by experiments.

A blackbody radiator is an idealized concept rather than a description of an actual radiator. Only a few surfaces, such as carbon black, carborundum, platinum black, and gold black, approach a blackbody in their ability to absorb incident radiant energy over a broad wavelength range. Many materials are spectrally selective in their ability to absorb and emit radiation, and hence they resemble blackbody radiators over some wavelength ranges and not over others. Over large ranges of the radio and infrared spectrum, planets behave as imperfect blackbodies. Later, we will see how the deviations from the blackbody spectrum contain information about physical and chemical properties of these distant objects.

An important property of a blackbody radiator is that its total radiant energy is a function only of its temperature; that is, the temperature of a blackbody radiator uniquely determines the amount of energy that is radiated into any frequency band. Planetary radio astronomers make use of this property by expressing the amount of radio energy received from a planet in terms of the temperature of a blackbody of equivalent angular size. This concept is developed more fully in the following paragraphs.

The German physicist Max Planck first formulated the theory that describes the wavelength dependence of the radiation emitted from a blackbody radiator in 1901. Planck's theory was revolutionary in its time, requiring assumptions about the quantized nature of radiation. Planck's radiation law states that the brightness of a blackbody radiator at temperature T and frequency v is expressed by

$$B = (2hv^3 / c^2)(e^{hv/kT} - 1)^{-1} \qquad (1)$$

where B is the brightness, watts per square meter per hertz per radian; h Planck's constant (6.63 x 10^{-34} J sec); v the frequency, hertz; $\lambda = c/v$ the wavelength, meters; c the velocity of light (3 x 10^{-8} m/sec); k Boltzmann's constant (1.38 x 10^{-23} J/K); and T the temperature, Kelvin.

Equation (1) describes how much power a blackbody radiates per unit area of surface, per unit frequency, into a unit solid angle. The curves in Fig. 1 show the brightness for three blackbody objects at temperatures of 6000, 600, and 60 K. The radiation curve for the undisturbed sun is closely represented by the 6000 K curve over a wide frequency range. The other two curves are representative of the range of thermal temperatures encountered on the planets. It should be noted in Fig. 1 that the brightness curve that represents the sun peaks in the optical wavelength range while representative curves for the planets peak in the infrared. This means that most of the energy received by the planets from the sun is in the visible wavelength range while that emitted by the planets is radiated in the infrared. Radio emissions are expected to play only a small role in the overall energy balance of the planets because the vast majority of the power that enters and leaves the planets is contained within the visible and infrared region of the spectrum.

FIG. 1. Blackbody radiation curves at 6000, 600, and 60 K. The 6000 K curve is representative of the solar spectrum.

A useful approximation to the Planck radiation law can be obtained in the low frequency limit where hv is small compared with kt ($hv << kT$). This condition is generally met over the full range of planetary temperatures and at radio wavelengths. It leads to the Rayleigh-Jeans approximation of the Planck law, given by

$$B = 2v^2kT/c^2 = 2kT/\lambda^2 \qquad (2)$$

The Rayleigh-Jeans approximation shows a linear relationship between physical temperature and the Planck brightness B. The brightness is also seen to decrease as the inverse square of the wavelength, approaching infinity as the wavelength gets shorter and shorter. The Planck brightness on the other hand reaches a maximum value at some wavelength, and then decreases at longer and shorter wavelengths. The Rayleigh-Jeans approximation matches the Planck law at wavelengths considerably longer than the wavelength of peak brightness. However for shorter wavelengths, the approximation gets progressively worse. At a temperature of 100 K and a wavelength of 1 mm, the error is ~8%.

Planetary radio astronomers estimate the radio power emitted by the planets by measuring with a radio telescope the power flux density received at the Earth. Figure 2 illustrates the geometry involved in the measurement of power from an ideal blackbody radiator. The spectral power (per unit frequency) emitted by an elemental surface element of the blackbody of area dA into a solid angle $d\,\Omega$ is given by $B\cos(\theta)\,d\Omega\,dA$, where θ is the angle between the normal to the surface and the direction of the solid angle $d\Omega$. The total power (per unit frequency interval) radiated by a blackbody radiator is obtained by integrating the brightness over the surface area and over the solid angle into which each surface element radiates. The total spectral power density produced by a spherical blackbody radiator of radius r at a distance d from the blackbody is given by

$$S = \frac{1}{4\pi d^2} \int\int B\cos(\theta)\, ds\, d\Omega \tag{3a}$$

$$= 2\pi kT(r/d)^2 / \lambda^2 \tag{3b}$$

The double integral represents integration over the surface area of the emitting body and over the hemisphere into which each surface element radiates. The quantity S is called "flux density." Flux density has units of power per unit area per unit frequency. A common unit of flux density is the flux unit (f.u.) or jansky (Jy), which has the value 10^{-26}W m^{-2} Hz^{-1}.

FIG. 2. Relationship between the brightness and power radiated by a blackbody spherical radiator of radius r and the flux density at a distance d from the blackbody.

If a planet radiates like a blackbody and subtends a solid angle of Ω steradians at the observer's distance, then the flux density produced by the planet is given by (using the Rayleigh-Jeans approximation)

$$S = 2kT\Omega / \lambda^2 \tag{4a}$$

$$= B\Omega \tag{4b}$$

The convention generally adopted for calculating Ω for a planet is to use the polar (PSD) and equatorial (ESD) semidiameter values in the expression

$$\Omega = \pi \times \text{PSD} \times \text{ESD} \tag{5}$$

The American Ephemeris and Nautical Almanac (AENA) provides values for PSD and ESD. A web site (http://ssd.jpl.nasa.gov) operated by the JPL Solar System Dynamics Group also provides these data. Equations (4) and (5) can be combined to yield the expression

$$S = 5.1 \times 10^{-34} T\theta_E\theta_P / \lambda^2 \text{ W m}^{-2} \text{ Hz}^{-1} \tag{6a}$$

$$= 5.1 \times 10^{-8} T\theta_E\theta_P / \lambda^2 \text{ Jy} \tag{6b}$$

where θ_E and θ_P are the apparent equatorial and polar diameters of the planets in seconds of arc and λ is in meters.

Even though the planets do not radiate like a blackbody, planetary radio astronomers express the observed brightness in terms of the temperature of an equivalent blackbody that would produce the same brightness. This temperature is called the brightness temperature T_B, defined as follows [from Eq. (4)]

$$T_B = B\lambda^2 / 2k = (S/\Omega)\lambda^2 / 2k \tag{7}$$

The brightness temperature for a planet can be calculated once the flux density S and solid angle Ω are known. The brightness temperature approximates the physical temperature the more the planet behaves like a blackbody radiator.

For problems that deal with the energy budget of the planets, it is necessary to know the total amount of power radiated over all frequencies. Once again the concept of the blackbody is useful. The Planck radiation law can be integrated over all frequencies and solid angles to obtain the relationship known as the Stefan-Boltzmann law, given by

$$R = \sigma T^4 \tag{8}$$

where R is the rate of emission, expressed in units of watts per square meter in the mks system. The constant σ has a numerical value of 5.67×10^{-8} W m^{-2} K^{-4}. Using the blackbody concept, we can now estimate the energy balance of planets that absorb visible light and radiate energy into the infrared.

B. Thermal Emission from Atmospheres and Surfaces

1. Effective Temperatures of the Planets

The amount of thermal radiation expected from a given planet depends in detail on the physical characteristics of the planet's atmosphere and surface. A starting point for

understanding the observed flux densities of the planets is to assume that the planets are blackbodies in equilibrium with the energy they receive from the sun and that which is radiated into free space. The radiation energy incident from the sun on a unit area per unit time is 1.39 x 10^3 W m^{-2} sec^{-1} at the Earth. This quantity is called the solar constant. The incident solar flux available to heat a planet is given by

$$(1 - A)S_0 \pi R^2 / d^2 \tag{9}$$

where A is the fraction of the incident solar flux that is not absorbed, πR^2 the cross sectional area of the planet, S_0 and d the mean distance of the planet from the sun in astronomical units. The quantity A is known as the Bond albedo or Russel-Bond albedo of the planet. Disregarding any significant internal heat sources or heating from charged particles, the total flux of absorbed radiation must equal the total flux of outgoing radiation when the planet is in equilibrium. The Stefan-Boltzmann law provides the relationship between effective temperature T_E and the absorbed flux:

$$\int \sigma T_E^4 \, ds = \pi R^2 (1 - A) S_0 / d^2 \tag{10}$$

If the planet rotates rapidly, equilibrium will be reached between the insulation and the radiation from the entire planetary surface area, $4\pi R^2$. This leads to the estimate

$$T_E = 277(1 - A)^{1/4} d^{-1/2} \text{ K} \tag{11}$$

If a planet did not rotate and its emitted radiation came only from the sunlit hemisphere, the effective temperature of the sunlit hemisphere would increase by the factor $2^{1/4}$ because of the reduction in the emission surface area. The equilibrium temperature for this case would become

$$T_E = 330(1 - A)^{1/4} d^{-1/2} \text{ K} \tag{12}$$

Figure 3 shows the calculated effective temperatures of the planets for the rapidly rotating and nonrotating cases. The albedos and distances used are those given in Table I. Having obtained the effective temperatures, it is possible to predict flux densities for the planets by using the effective temperatures from Eq. (11) or (12) and the angular diameter data for the planets in Table I in Eq. (6a) or (6b).

FIG. 3. Theoretical effective temperatures of the planets for two models. The higher-temperature model is for the case where the

planet is not rotating [Eq. (12)]. The lower-temperature model is for the case where the planet is rapidly rotating [Eq. (11)].

Thus far, we have discussed the ideal model in which the planets behave like blackbody radiators. This gives planetary astronomers a crude model from which they can estimate flux densities and search for departures. The planets would not be very interesting to study if they behaved like blackbodies since a single parameter, namely the temperature, could be used to define their radiation properties. More important, it is the departures from the simple model that allows radio astronomers to deduce the physical properties of the planets.

The observed temperatures of the planets depart markedly from this ideal model for a number of different reasons. The presence of atmospheres on the planets produces strong perturbations from the ideal model. Atmospheres modify the amount of heat that enters and leaves the planets over the entire electromagnetic spectrum. Strong "greenhouse" effects can raise the temperatures considerably over that calculated from the ideal models. The presence of internal sources of energy within a planet can modify its effective temperature and affect the thermal profile of the atmosphere. Surface emissivity effects modify the apparent temperature of the planets. Nonuniform heating of the planets by the sun, due to orbit eccentricity and rotational effects, also produces departures from the ideal model. Nonthermal emission from planetary magnetospheres produces the largest departures from the blackbody model. The role of the planetary astronomer is to sort out the various effects that take place and to measure and infer the actual physical characteristics of the planets.

2. Radiative Transfer in Planetary Atmospheres

The apparent brightness temperature of a deep atmosphere is related to the physical parameters of the atmosphere, such as pressure, temperature, and composition, through the equation of radiative transfer. To a good approximation at radio wavelengths, the equation of radiative transfer for a ray making an angle $\cos^{-1}\mu$ with the vertical in a lossy medium is

$$T_B(\nu,\mu) = \int T(z) \times \exp\left[-\int \alpha(z',\mu)\mu^{-1}dz'\right] \alpha(z,\nu)\mu^{-1}\,dz \qquad (13)$$

where $\alpha(z, \nu)$ is the absorption per unit length of the atmosphere at frequency ν and depth z and $T(z)$ the physical temperature along the line of sight. This equation states that the brightness temperature in any given direction is the sum of the radiation emitted at each point along the trajectory, each component being attenuated by the intervening medium. The equation neglects scattering and variations of the index of refraction. These effects are important in certain

wavelength ranges and for certain ray trajectories. Sometimes it is necessary to add another term to Eq. (13) to account for the presence of a solid surface.

Measurements with single-dish antennas generally have insufficient angular resolution to determine the brightness distribution across the planetary disk. The mean disk brightness temperature T_D can be calculated by integration of Eq. (13) over all angles of incidence. This yields

$$T_D(\nu) = 2\int_0^1 T_B(\nu,\mu)\mu\, d\mu \tag{14}$$

This equation is usually used to calculate the average disk brightness temperature for a model atmosphere for comparison with observations. Unlike the blackbody radiation model, this model predicts a wavelength dependence of the brightness temperature. The frequency dependence is introduced by the frequency dependence of the absorption and the thermal gradients in the atmosphere.

The absorption may either vary slowly with frequency or exhibit an abrupt change over a narrow frequency range. The two kinds of absorption are referred to as nonresonant and resonant absorption, respectively. The standard classical theory of nonresonant molecular absorption is due to Debye. Resonant absorption is produced by the discrete transitions from one energy level to another in a molecule that cause the molecule to absorb or emit at particular frequencies. The study of resonant absorption lines in planetary atmospheres is referred to as planetary spectroscopy.

A brief discussion of the energy levels in the molecule CO is helpful in understanding resonant absorption and the usefulness of planetary spectroscopy as a tool for studying planetary atmospheres. The rotational energy levels in CO are quantized according to the relation

$$E_r = J(J+1)B \tag{15}$$

where J ($J = 0, 1, 2, \ldots$) is the rotational quantum number and B the rotational constant. The rotational constant for a diatomic molecule is defined by

$$B = h^2 8\pi^2 I \tag{16}$$

where I is the moment of inertia of the molecule about the axis perpendicular to the line connecting the nuclei and h is Planck's constant. The transitions between the various energy levels are limited by the exclusion principle to $\Delta J = \pm 1$. The energy of a quantum emitted or absorbed during a transition is given by

$$h\nu = J(J+1)B - (J-1)(J)B = 2JB \tag{17}$$

When B is expressed in megahertz, the transition frequency ν in megahertz is expressed directly as $2JB$. The value of B for CO is 57,897.5 MHz. Thus, CO has two rotational transitions in the millimeter spectrum, a ground state (~115 GHz) and the first excited state (~230 GHz). The ground state transition corresponds to a transition between $J = 0$ and 1; the first excited state corresponds to a transition between $J = 1$ and 2. Both of these transitions have been observed in the atmospheres of Venus and Mars.

A number of factors cause the energy levels in a molecule to vary slightly and cause the molecule to emit or absorb over a range of frequencies. The range of frequencies or "width" of a spectral line is determined primarily by three factors: (1) natural attenuation, (2) pressure broadening, and (3) Doppler broadening. Pressure broadening and Doppler broadening are the dominant mechanisms in most planetary astronomy applications. Natural attenuation is interpreted as the disturbance of the molecule by zero-point vibration of electromagnetic fields, which are always present in free space.

Doppler broadning is caused by the frequency shift introduced by the molecule's motion. The statistical effect of the simultaneous observation of a large number of molecules moving at various velocities is to spread the frequency of the spectral line over a range of frequencies. The spectral line produced by thermal motions in a gas (in thermodynamic equilibrium) is symmetric and has a full width at half-maximum of

$$\Delta\nu = 7.2 \times 10^{-7}(T/M)^{1/2}\nu \tag{18}$$

where T is the temperature of the gas, M the molecular weight of the molecule, and ν the frequency of the spectral line without Doppler shift. The Doppler linewidth of the ground state transition ($J = 0$ to 1) of CO at 200 K is ~200 kHz. A measure of the Doppler width can be used to estimate the temperature of the gas.

Pressure broadening can be interpreted as the effect of collisions disrupting the processes of emission and absorption in a molecule. A number of different theoretical line shapes have been derived to explain pressure broadening. The one most widely used is the Van Vleck-Weisskopf line shape. Linewidths due to pressure broadening are proportional to pressure, the proportionality constant depending on the particular molecules involved in the collisions. For CO broadened by CO_2, the linewidth of the ground state transition of CO is approximately

$$\Delta\nu = 3.3p(300/T)^{0.75} \tag{19}$$

where p is the pressure in millibars and Δv the linewidth in megahertz. At a pressure of 1 mbar and temperature of 200 K, the pressure-broadened linewidth of CO is ~4.5 MHz. Observations of pressure-broadened spectral lines can be used to determine the altitude distribution of a molecule in a planetary atmosphere.

3. Radiative Transfer in Planetary Subsurfaces

While some planets have deep atmospheres, others such as Mercury and Mars have relatively tenuous atmospheres. For these planets (and the moon and satellites) the atmospheres are nearly transparent at radio wavelengths, except possibly in narrow wavelength ranges, where resonant absorption lines can produce strong absorption. Thermal emission from the surfaces of these planets is easily observed at radio wavelengths; it is possible to interpret the measurements in terms of the physical properties of the near-surface materials.

Observations of the thermal radiation at radio wavelengths provide measurements that are complementary to infrared measurements of the subsurface materials. Thermal emission in the infrared is emitted very close to the surface of the planet because the opacity of most minerals is high at infrared wavelengths. Consequently, infrared thermal emission reflects the physical characteristics of the near-surface materials. The opacity of typical planetary materials is considerably less at radio wavelengths, and the observed thermal emission originates at greater depth.

The interpretation of thermal emission data from a planetary surface begins with an analysis of heat transfer in solids. The solid surface receives heat from the incoming solar radiation and transports it downward, mainly by conduction and radiation. Boundary conditions are set by the heating of the surface by the sun, the nighttime cooling, and the internal sources of heat, if any. The surface temperature responds to the heating and cooling, being controlled by the "thermal inertia" of the near-surface material. Because the planets are heated and cooled periodically due to their spin, a thermal wave is set up in the surface layers. The equation of radiative transfer is used to relate the temperature structure in the subsurface layers to the observed thermal emission.

The formal solutions of the equations of heat transfer in solids and radiative transfer depend on the following properties of the near-surface material: the complex dielectric constant $\varepsilon(\lambda)$, thermal conductivity k (ergs per centimeter per second per Kelvin), specific heat c (ergs per gram per Kelvin), and density ρ (grams per cubic centimeter). The analytic theory of heat transfer at planetary surfaces begins by assuming that the temperature at any point on the surface can be expanded in a Fourier series in time:

$$T_s(t) = T_0 + \sum_{n=1}^{\infty} T_n \cos[(nwt) - \Phi_n] \tag{20}$$

where ω (radians per second) is the fundamental heating frequency (i.e., rotation rate of the planet as seen from the sun) and t is time. Assuming that the planet is a semi-infinite homogeneous slab with constant thermal properties, the equilibrium solution for the subsurface temperature distribution is

$$T(x,t) = T_0 + \sum_{n=1}^{\infty} T_n \exp(-x\beta_n) \cos \times [(wt - \beta_n x - \Phi_n)] \tag{21}$$

where x is the depth beneath the surface and β_n is given by

$$\beta_n = [n\omega\rho c / 2k]^{1/2} = \beta_1 n^{1/2} \tag{22}$$

Equation (21) represents a series of thermal waves propagating into the surface and attenuating with distance. The higher harmonics are attenuated more rapidly than the lower harmonics since β_n increases as the square root of the harmonic number n. The attenuation and phase of each harmonic depend on the quantity β_1, which is termed the "thermal absorption coefficient" of the planetary material. The reciprocal of β ($L_t = 1/\beta_1$) is termed the "thermal skin depth." At a distance of 3 to 4 thermal skin depths, the fluctuations in subsurface temperature are practically zero.

Given the thermal absorption coefficient and the boundary conditions on the heating, it is possible to determine the constants of temperature (T_0 and T_n) and phase (Φ_n) in Eq. (21). The inverse problem is faced by the radio astronomer, namely to determine the thermal absorption coefficient from measurements of the thermal emission. This is done in the following manner. The temperature distribution given by Eq. (21) is used in the equation of radiative transfer

$$T_B = [1 - R_P(v,\theta_0)] \int_0^{\infty} T(x) \exp \times [-k_v x / \cos(\theta_i)][k_v / \cos(\theta_i)]\, dx \tag{23}$$

to compute the radio brightness temperatures at any wavelength for comparison with observations. In this expression k_v is the power absorption coefficient at frequency v, θ_i the angle of incidence of radiation just below the surface, and θ_0 the angle of incidence of the observation. The function R_P (v, θ_0) is the Fresnel reflection coefficient of polarization P emerging at angle θ_0.

After substituting (the series) Eq. (21) for $T(x, t)$ in Eq. (23), the integral can be evaluated as a series of integrals. Each integral can be put in the form of a standard Laplace transform and integrated directly. The resulting brightness temperature at time t at a specified point on the surface is given by

$$T_B(v,p,t) = [1 - R_P] \sum_{n=1}^{\infty} \frac{T_n \cos[nwt - \Phi_n - \Psi_n(\theta_i)]}{[1 + 2\delta_n(\theta_i) + 2\delta_n 2(\theta_i)]^{1/2}} \tag{24}$$

where

$$\delta_n(\theta_i) = n^{1/2}\,\beta_1\,\cos(\theta_i)/k_v \tag{25}$$

$$\Psi_n = \tan^{-1}\{\delta_n[\theta_i/(1+\delta_n(\theta_i))]\} \tag{26}$$

Defining $1/K_v$ as the radio absorption length (L_e), δ_1 reduces to the ratio of the radio absorption length to the thermal absorption length at normal incidence. Equations (24)–(26) relate the observational data to the physical parameters of the surface materials. Only the first few terms of Eq. (24) are normally important because the higher-order terms are small. The most important terms determined from the observations are δ_1 and Ψ_1. The δ_1 term defines the reduction in amplitude of the fundamental diurnal wave component from its surface value. It is best determined from observations at several different wavelengths spanning a wavelength range of 2:1 or more. The Ψ_1 term defines the phase shift in the diurnal wave at depth. It also can be deduced from measurements at several wavelengths, but usually with somewhat less precision than δ_1.

The parameter δ_1 can be written in terms of the physical characteristics of the surface material as follows:

$$\delta_1 = L_e L_t = (\Omega\rho c/2k)^{1/2}\lambda[2\pi\sqrt{\varepsilon}\tan(\Delta)]^{-1} \tag{27}$$

where $\tan(\Delta) = 2\sigma/\varepsilon_r\,v$ is the loss tangent, ε_r the real part of the dielectric constant, and σ the electrical conductivity (mhos per meter) of the medium.

Radio observations by themselves do not permit separation of the physical parameters contained in δ_1 and Ψ_1. Nevertheless, the radio data, when combined with infrared data, radar data, and laboratory data for real materials, constrain the material properties and in some cases allow one to exclude certain classes of materials in favor of others.

C. Nonthermal Radio Emission

Thermal radio emission in solids and neutral gases arises from the emission of quanta from individual atoms and molecules in thermodynamic equilibrium with each other. Random collisions between ions and electrons in thermal equilibrium with each other in an ionized gas also produce thermal emission. The electrons and ions in this case have a Maxwellian velocity distribution. When energy sources are present that produce particles having a non-Maxwellian velocity distribution, the system is not in thermodynamic equilibrium. Efficient processes can arise under these conditions that produce large amounts of radio energy. Nonequilibrium

conditions frequently arise in an ionized gas or plasma typical of those found in space. In a fully ionized gas, nonequilibrium conditions can lead to coherent and incoherent plasma emissions. The radiation that arises from these mechanisms is called nonthermal emission. Cyclotron emission and synchrotron emission are examples of nonthermal emission. In the case of thermal emission, the blackbody radiation laws limit the radiation to an amount corresponding to the temperature of the body. For nonthermal radiation, this limit does not exist. The brightness temperature of nonthermal radiation sometimes exceeds millions of degrees even though the effective temperature of a planet does not exceed several hundred degrees.

The classic sources of nonthermal radio emission within the Solar System are Jupiter's magnetosphere and the solar corona. Nonthermal radio emission have also been observed from the Earth's magnetosphere, and the other three giant planets, Saturn, Uranus, and Neptune. The emissions from the latter planets can only be observed from spacecraft near the planets. Cyclotron and coherent plasma emission account for much of the low frequency (<10 MHz) nonthermal emission from these planets and the solar corona. This emission is highly variable and the details of the generation processes involved are not clearly understood.

Synchrotron radiation is the dominant source of emission from Jupiter from about 50 MHz to 5 GHz; it also accounts for continuum bursts of type IV from the sun. The theory of synchrotron radiation is well developed. A review article on magnetospheric radio emissions by Carr, Desch, and Alexander, contained in the book by Dessler cited in the bibliography, lists a number of references.

High-energy electrons moving in a magnetic field produce synchrotron radiation. Although the observed synchrotron radiation from a planet or the sun is the integrated emission from many electrons, an understanding of the radiation characteristics of a single electron in a magnetic field is sufficient to understand the qualitative aspects of the observations.

A single charged electron moving in a magnetic field is accelerated unless its velocity is solely in the direction of the magnetic field. This causes the electron to emit electromagnetic waves. The nature of these waves depends on whether the electron is nonrelativistic (velocity $<<3 \times 10^{10}$ cm/sec) or relativistic (velocity $\sim 3 \times 10^{10}$ cm/sec). The radiation emitted by nonrelativistic electrons is referred to as cyclotron radiation; radiation emitted by relativistic electrons is referred to as synchrotron emission.

A nonrelativistic electron with mass m and charge e, in the presence of a magnetic field (of magnitude B), moves in a helical path with the sense of rotation of a right-hand screw advancing in the direction of the magnetic field. The frequency of rotation about the magnetic field, sometimes called the electron cyclotron frequency or the gyrofrequency, is given by

$$f_c = Be/2nm = 2.8B(\text{gauss})\text{MHz} \qquad (28)$$

Cyclotron radiation is emitted in all directions and has a frequency equal to the gyrofrequency. The radiation is polarized with the polarization depending on the direction of propagation. The polarization is circular when viewed along the direction of the magnetic field and linear when viewed in the plane of the orbit. At intermediate angles the polarization is elliptical.

Relativistic electrons radiate not only at the gyrofrequency but also at the harmonics. The relativistic mass increase with energy causes the harmonic spacing to decrease with increasing energy until the synchrotron spectrum is essentially smeared into a continuum. The radiation from a relativistic electron is highly nonisotropic. The emitted radiation is concentrated within a narrow cone about the instantaneous direction of the velocity vector with an approximate half cone width given by

$$\theta \cong mc^2 / E \text{ rad} \tag{29}$$

where E is the electron energy. When E is expressed in millions of electron volts (MeV) and θ in degrees, the expression becomes

$$\theta \cong 29 / E(\text{MeV}) \text{ deg} \tag{30}$$

An observer situated in the plane of the electron orbit would see one pulse per revolution of the electron. These pulses recur at the relativistic gyrofrequency of the electron.

A single electron of energy E radiates synchrotron emission with an intensity spectrum that varies as $\nu^{1/3}$ (ν is frequency) up to a critical frequency $0.29\nu_c$ and decreases exponentially at higher frequencies. The critical frequency is defined as

$$\begin{aligned} \nu_c &= (3e / 4\pi mc)(E / mc^2)B \\ &= 16.08\, B(\text{gauss})\, E^2(\text{MeV}) \text{ MHz} \end{aligned} \tag{31}$$

Thus a 10-MeV electron in a 1-gauss magnetic field will radiate a maximum intensity near 0.29 x 1608 MHz. The spectral density of the radiation near the frequency of the maximum intensity is

$$I(\nu = 0.29\nu_c) \cong 2.16 \times 10^{-29}\, B(\text{gauss}) \text{ W/Hz} \tag{32}$$

The total energy radiated per second is given by

$$P = 6 \times 10^{-22}\, B^2(\text{gauss})\, E^2(\text{MeV}) \sin^2 \alpha \text{ W} \tag{33}$$

where α is the pitch angle of the electrons ($\alpha = 90°$ for electrons with no motion in the direction of the magnetic field).

As in the case of nonrelativistic electrons, the polarization is linear when the electron orbit is seen edge-on and elliptical or circular elsewhere. Since the intensity of the radiated power is beamed in the plane of the orbit, synchrotron radiation is predominantly linearly polarized.

FIG. 4. Basic components of a simple radio telescope.

It is possible to deduce many properties of Jupiter's magnetic field and of the high-energy particle environment from radio measurements of Jupiter by judicious use of the equations given above. Detailed calculations of synchrotron emission are complex since they involve integrals over the volume of the emitting electrons and over the electron energy spectrum while taking into account the complex geometry of the magnetic field and polarization properties of the radiation.

III. INSTRUMENTATION FOR PLANETARY RADIO ASTRONOMY

A radio telescope is a device for receiving and measuring radio noise power from planets, satellites, asteroids, and comets as well as from galactic and extragalactic radio sources. A simple radio telescope consists of an antenna for collecting the noise power (in a specified bandwidth, polarization and from a limited range of directions) and a sensitive receiver-recorder for detecting and recording the power. The antenna is analogous to the objective lens or primary mirror of an optical telescope; the receiver is analogous to the recording medium of the optical telescope (i.e., photographic plate, photodetectors, etc.). Figure 4 shows the basic components and configuration of a simple radio telescope. Single antennas may be connected together electrically to form an "array" radio telescope which has greater sensitivity and directivity than a single antenna. There are many different types of radio telescopes in use today and their capabilities and visual appearances show much diversity.

Three important properties of an antenna are its effective area A_e (θ, ϕ), normalized antenna power pattern $P_N(\theta, \phi)$, and gain G. The effective area is a measure of the wave front area from which the antenna can extract energy from a wave arriving at the antenna from different directions. It can be thought of as the equivalent cross section of the antenna to the incident wave front. For most radio telescopes, the effective area is less than the physical area. A working definition of the effective area is given by

$$P = \frac{1}{2} S A_e \, dv \tag{34}$$

where P is the power the antenna can deliver to a matched load in bandwidth dv when flux density S is incident on the antenna. The factor 1/2 is introduced because it is assumed that the radiation is unpolarized and that the antenna is responsive to only one polarization component.

The effective area of an antenna is a function of the direction of arrival of the waves. The effective area to a signal from a distant transmitter, as a function of direction, is called the antenna power pattern. The effective area normalized to unity in the direction of the maximum effective area A_{e-max} is the normalized power pattern of the antenna:

$$P_N(\theta, \phi) = A_e(\theta, \phi) / A_{e-max} \tag{35}$$

By reciprocity arguments, the normalized power pattern is the same for both transmitting and receiving.

A general expression for the power delivered to a radio receiver from a planet is obtained by integrating the brightness over the solid angle of the planet and over the bandwidth of the receiver as given below:

$$P = \frac{1}{2} \int \int \int B(\theta, \phi, v) \times A_e(\theta, \phi, v) \sin(\theta)\, d\theta\, d\phi\, dv \tag{36a}$$

$$P = \frac{1}{2} A_{e-max} \int \int \int B(\theta, \phi, v) \times P_N(\theta, \phi, v) \sin(\theta)\, d\theta\, d\phi\, dv \tag{36b}$$

A typical antenna power pattern consists of a large number of lobes with one or a few lobes being much larger than the others, as shown in Fig. 5. The lobe with the largest maximum is called the main lobe, while the remaining lobes are called side or back lobes.

FIG. 5. Antenna power pattern and its relation to a measurement of the flux density from a planet.

The half-power beamwidth of the main lobe, Θ, is the angle between the two directions in which the received power is half of that in the direction of maximum power. The half-power beamwidth is a measure of the ability of the antenna to separate objects that are close together in angle. In optical systems, this is known as resolving power. An estimate of the beamwidth in radians of the main lobe is given by $\Theta \sim \lambda/D$, where D is the linear dimension of the antenna in the plane in which the beam is measured and λ the wavelength in the same units as D. The resolving power can be improved by using either a shorter wavelength or a larger-diameter telescope.

Two major classifications of large radio telescopes are (1) filled-aperture telescopes and (2) unfilled-aperture telescopes. Filled-aperture radio telescopes generally consist of a single

reflecting element that focuses the received radio waves to a point or, in some cases, along a line. Examples of filled-aperture radio telescopes are the 64-m parabolic reflector antenna at Parkes, Australia, the 100-m parabolic reflector at Bonn, Germany, and the ~300-m spherical reflector antenna at Arecibo, Puerto Rico. The newest of the large filled-aperture radio telescopes is the 100-m Green Bank Telescope (GBT). The surface panels of the GBT are supported by motor driven actuators to compensate for the structural deformations of the antenna. The GBT is expected to operate at frequencies up to 80 GHz under the most favorable conditions available at the site.

The resolving power of most filled-aperture radio telescopes are generally less than is required for adequate resolution of the disks of the planets. The few exceptions are the large telescopes such as the GBT and the 30m Pico Villeta telescope which operate at short millimeter wavelengths. The largest single-dish antennas presently available to radio astronomers are capable of partially resolving the disks of the planets of largest angular diameter, Venus and Jupiter. For example, an antenna with a maximum dimension of 100 m operating at a wavelength of 10 cm would have a main lobe width of approximately 1/1000 radians or 3.44 arc min. The angular diameters (Table I) of Venus and Jupiter are approximately 1 arc min; thus an antenna with an aperture of ~344 is required just to "fill the main lobe." Adequate resolution of even the largest planets (at 10-cm wavelength) requires apertures at least 10 times larger.

Higher resolving power can be achieved by connecting together electrically the outputs of two or more filled-aperture antennas to the input of a common radio receiver. The resolving power of such a system depends on the maximum separation between the individual elements, even though the space between the elements is unfilled. Multiple-element radio telescopes (arrays), with spaced separations between the elements to achieve high resolving power, are termed unfilled-aperture radio telescopes. The simplest unfilled-aperture radio telescope is a total power interferometer with two identical elements, as shown in Fig. 6. The output from the two-element interferometer modifies the power pattern of a single element with an angular modulation of scale λ/D superimposed.

FIG. 6. Total power interferometer. (Top) Geometry of a two-element interferometer. (Bottom) Antenna response for a single element of the interferometer (left) and response of the interferometer (right) to a completely unresolved planet.

The Very Large Array (VLA) radio telescope, located on the plains of San Augustin west of Socorro, New Mexico, is a classic example of an unfilled-aperture radio telescope. This instrument, completed in early 1981, is especially important to planetary radio astronomers. The

VLA consists of 27 antennas, each having a diameter of 25-m. The individual antennas are arranged in a huge Y shaped pattern. The antennas are mounted on tracks so that they can be moved into four configurations along the Y-shaped baseline. This allows the radio telescope to be custom tailored to a particular kind of measurement. The maximum antenna separation is 36 km across. At the highest frequency (43 GHz), the VLA has a resolution of .043 arc seconds. The effective sensitivity is equivalent to a filled aperture telescope having a diameter of 130 m. Continuum, polarization, and spectral line observations at eight wavelength bands (0.7, 1.3, 2.0, 3.6, 6, 20, 90, and 405 cm) are supported. The VLA has sufficient resolving power to measure the brightness distributions across all of the planets at its shortest wavelengths.

Small arrays at millimeter wavelengths have been operational for over a decade and have returned many interesting continuum and spectroscopic images of the planets. Major millimeter arrays are BIMA millimeter array, Owens Valley Radio Observatory (OVRO) millimeter array, Plateau de Bure Observatory, and Nobeyama Millimeter Array (NMA). The BIMA and OVRO millimeter arrays are likely to be combined into a single large millimeter array in the future. The Submillimeter Array(SMA) is an exploratory instrument for high resolution observations at submillimeter wavelengths. The SMA will initially consist of eight 6-m antennas sited on Mauna Kea at an elevation of 4050 meters. A major step in millimeter Solar System research will be provided by the construction of very large millimeter arrays. Two large arrays are currently in their early phases. The Atacama Large Millimeter Array (ALMA) will consist of 64 (or more) 12-m antennas located at an elevation of 16,400 feet in Llano de Chajnantor, Chile. This array will provide imaging in all atmospheric windows between 1 cm and 350 microns. The array configuration will provide baselines ranging from 150 m to 10 km. Spatial resolution of 10 milliarcseconds, 10 times better than the VLA will be possible. A Large Millimeter and Submillimeter Array (LMSA) has been proposed in Japan. This array will consist of 50 10-m antennas and will cover frequencies from 80 to 800 GHz. These new very large arrays will open up many possibilities for planetary radio astronomers. Imaging of planetary atmospheres will be greatly improved. General circulation studies will be greatly enhanced. Planetary satellites will be easily resolved making temperature and wind measurements possible. Imaging and spectroscopy of comets will be greatly improved and many new molecules can be studied.

The performance of a filled-aperture antenna is sometimes expressed by specifying the gain of the antenna. The antenna gain is a measure of the ability of the antenna to concentrate radiation in a particular direction. Gain is defined as the ratio of the flux density produced in direction (θ, ϕ) by an antenna when transmitting with an input power P to the flux density produced by the same transmitter feeding an antenna that radiated equally in all directions. The antenna gain, effective area, and beam solid angle (Ω) are interrelated quantities. The relationship between them is given by

$$G = 4\pi A_{e-max} / \lambda^2 = 4\pi / \Omega \tag{37}$$

Radio astronomers generally specify the received power P delivered to the receiver in the frequency bandwidth dv as the antenna temperature T_a, defined by

$$T_a = P / k\, dv \tag{38}$$

where k is Boltzmann's constant. This definition follows from the Nyquist theorem, which states that the noise power delivered from a resistor at temperature T into a matched load in bandwidth dv is

$$P_N = kT\, dv \tag{39}$$

The antenna temperature can be thought of as the physical temperature at which a resistor would have to be maintained to deliver the same power to the receiver as the antenna.

The antenna temperature can be thought of as the physical temperature at which a resistor would have to be maintained to deliver the same power to the receiver as the antenna.

The antenna temperature of an unresolved radio source can be calculated directly from the definition of the effective area and the definition of antenna temperature if its flux density is known. For a planet of known solid angle and temperature, the antenna temperature can be calculated by substituting the Rayleigh-Jeans approximation for the brightness, $B = 2kT_p/\lambda^2$, and the relationship between effective area and beam solid angle.

$$A_{e-max} = \lambda^2/\Omega \tag{40}$$

into Eq. (36). When the planet is unresolved by the main beam of the telescope, the antenna temperature is given by

$$T_a = (\Omega_p / \Omega) T_p \tag{41}$$

where Ω_p and T_p are the solid angle and temperature of the planet, respectively, and Ω is the beam solid angle of the telescope. The relationship states that the antenna temperature of a planet is proportional to the brightness temperature of the planet with the constant of proportionality being the ratio of the solid angle of the planet to the solid angle of the beam. This approximation holds when $\Omega_p << \Omega$; consequently, the antenna temperature is always less than the brightness temperature.

The concept of specifying the received power in terms of an equivalent temperature is useful for estimating the signal-to-noise ratio for a particular measurement since random noise in the receiving equipment is easily expressed as a temperature. A discussion of signal-to-noise ratio follows.

B. Radio Receivers

Radio astronomy receivers, like ratio telescopes, are highly varied, depending on the type of measurement to be performed. The function of the receiver is to detect and measure the radio emission with as much sensitivity as possible. The receiver also defines the frequency range or ranges of the measurement. Most modern receivers consist of a low-noise amplifier to boost the power of the incoming signal (without adding significant noise), followed by a heterodyne mixer and square law detector. The heterodyne mixer transforms the signal frequency to a convenient (often lower) frequency for detection or further processing. or high resolution spectroscopic observations, the square law detector may be preceded by spectrometer, such as a filter bank, digital autocorrelator, or acousto-optical-spectrometer.

The inherent noise fluctuations of a radio receiver usually determine the weakest signal strength that can be measured with a radio telescope. The statistical nature of noise radiation is such that statistical fluctuations are proportional to the noise power itself. Furthermore, the average of N independent measurements of the noise power is $\sqrt{N}$ times more accurate than a single measurement. Noting that a single independent measurement can be made in the minimum time interval, $1/dv$, the maximum number of independent measurements that can be made in time t is $t\ dv$. Thus, the sensitivity equation for an ideal receiver is given by

$$\Delta T = \text{rms noise power} \approx T_S /(t\ dv)^{1/2} \tag{42}$$

where the "system temperature" T_S is a measure of the noise power from the receiver and t is the integration time of the measurement. The rms noise power is expressed in Kelvin and can be directly compared with the antenna temperature to determine the signal-to-noise ratio (SNR) of a particular measurement.

A modern radio telescope may have a system temperature of 20 K or less in the frequency range 1–10 GHz, where the radiation from the terrestrial atmosphere and galaxy are both low. Noise temperatures in the millimeter and submilliter bands are substantially higher. For measurements of the radio continuum, dv may be chosen to be 10 MHz or larger, depending on the characteristics of the radio receiver being used. If we adopt a value of 100 MHz for dv and 20 K for T_S, then the rms noise power obtained in 1 sec of integration is 0.002 K. For planetary spectroscopy, dv would have to be reduced to 1 MHz or less and the rms noise power would

increase to 0.02 K. These noise fluctuations can be further reduced by increasing the integration times; however, systematic effects within the receiving equipment prevent ΔT from being pushed to zero.

C. Spacecraft

Earth-based radio observations of the planets have limitations which affect certain types of measurements. These limitations include (1) the inability to obtain spatial resolution on scales of a few meters or less, (2) restrictions on the viewing geometry of the planets, (3) limitations set by the opaqueness and variability of the terrestrial atmosphere, (4) an intrinsic faintness of the radio emissions from planetary bodies, and (5)interference from man-made radio noise. The opacity of the terrestrial atmosphere varies with frequency. The atmosphere is opaque at frequencies lower than about 5 MHz due to the terrestrial ionosphere. Attenuation due to the atmospheric gases, water vapor, and oxygen affects the centimeter, millimeter, and submillimeter bands but observations are possible from the ground by working in the transparent "windows' in the spectrum. Rain, fog, and clouds occasionally limit the usefulness of the centimeter and millimeter bands.

To overcome these difficulties, a number of spacecraft radio instruments have been proposed, and several have flown on U.S. spacecraft. The first planetary radio system on a U.S. spacecraft was a two-channel microwave radiometer that operated at wavelengths of 13.5 and 19.0 mm, flown on the *Mariner II* spacecraft to Venus in 1962. The microwave radiometer system weighed ~10 kg and used an average power of 4 W. This early system was designed to take advantage of the high spatial resolution and sensitivity that could be achieved from a spacecraft. Another radio astronomy experiment was placed on the Voyager spacecraft that was launched in the late 1970s to the outer planets and targeted to fly by Neptune in 1989. This experiment measures the radio spectra of planetary emissions in the range 1.2 kHz to 40.4 MHz. The system was designed to measure planetary spectra below the frequency range that is cut off by the Earth's ionosphere and to take advantage of the unique viewing geometry provided by the spacecraft. The Magellan Venus orbiter spacecraft carried a 12.6 cm radio receiver which allowed over 91% of its surface to be measured.

In the future, we expect to see many more radio astronomy spacecraft experiments. Spacecraft experiments will allow the submillimeter spectral range to be observed without hindrance from the terrestrial atmosphere. Planetary spectroscopy in the submillimeter spectral range is expected to reveal new information about the upper atmospheres of the planets. The ESA ROSETTA spacecraft will carry a millimeter and submillimeter wave spectroscopic instrument (MIRO) to investigate the nucleus and coma of a comet.

IV. RESULTS—PLANETS AND COMETS

A. Mercury

Radio measurements of Mercury show no evidence of an atmosphere. Estimates based on other techniques including spacecraft flyby instruments show the atmosphere on Mercury to be extremely tenuous, with a surface pressure of $\sim 5 \times 10^{-15}$ bar. For the purpose of interpreting the radio data, it can safely be assumed that Mercury is an airless planet. The radio emission from Mercury is thermal in character, strongly controlled by the high eccentricity of Mercury's orbit and the synchronism between Mercury's spin period and its period of revolution. Solar tidal effects have caused the period of axial rotation of Mercury to be 58.642 days, precisely two-thirds of its orbital period of 87.97 days. One solar day on Mercury is equal to 3 stellar days or 2 Mercurian years. This period equals 176 mean Earth solar days. Because of the synchronism between spin period and revolution period, the sun takes a curious diurnal path in the sky as seen from the surface of Mercury (Fig. 7). At some longitudes, the sun rises and sets twice a Mercury day. At perihelion the insolation is approximately twice its value at aphelion. The insolation reaches a maximum value of $\sim 14 \times 10^3$ W/m^2, 10 times the value of Earth. The visual albedo of Mercury is similar to that of the moon. The spin-orbit coupling and eccentricity combine to cause the surface of Mercury to be heated very nonuniformly in longitude. A pair of longitudes 180° apart alternatively faces the sun at perihelion. These longitudes are preferentially heated because their midday insolation occurs when the sun is nearly stationary on the meridian and the sun-Mercury distance is at a minimum. At longitudes 90° away from these hot longitudes, the heating is identical but much less than that received at the hot longitudes. The longitudinal temperature variations on Mercury are indicated schematically by the "hot," "warm," and "cold" regions shown on the left in Fig. 7. This pattern of temperature variations is fixed on Mercury because the spin-orbit coupling causes the heating to be cyclic at each longitude (i.e. the same pair of longitudes faces the sun at perihelion).

FIG. 7. (Left) Diurnal path of the sun about Mercury and (right) representative brightness temperature curves near 4 cm wavelengths for "hot," "warm," and "cold" regions on Mercury.

The solar heating cycle on Mercury suggests that the two longitudes that see the sun directly overhead at perihelion (receiving more than twice as much energy as the longitudes 90° away) will be hotter than those 90° away. This is borne out by the radio observations. The right-hand

portion of Fig.7 shows a schematic representation of the variation of temperature at "hot," "warm," and "cold" regions on Mercury at a wavelength near 4 cm. Most of the older, single dish microwave observations of Mercury do not have sufficient resolving power to resolve the disk of Mercury, so the reported temperatures are averages over the entire visible disk.

Radio images of the planet have been obtained with the VLA and the BIMA array. Such images clearly show the brightness variation across the disk of Mercury. At short wavelengths, where shallow layers are probed, the temperature is usually highest at local noon. However, when deeper layers are probed, the diurnal heating pattern is less obvious, and one sees the two hot regions. Fig. 8 (left side) shows a radio image at 3.6 cm. At this wavelength one probes ~70 cm into the crust. The hot region at longitude 0° is clearly visible on the night side, while the high temperature on the day side is caused both by the 180° hot longitude and solar insolation. Mercury's hot and cold longitudes have been modeled in detail. The image on the right shows residuals after a thermal model was subtracted from the image on the left. Most remarkable here are the negative temperature differences near the poles and along the terminator, suggesting that the poles and terminator are colder than predicted by the model. This is likely caused by surface topography, which causes a permanent shadowing effect at high latitudes and transient effects in the equatorial regions, where crater floors and hillsides are alternately in shadow and sunlight as the day progresses. Some crater floors near the poles are permanently shadowed, and radar observations have revealed evidence for the existence of water ice at such crater floors.

Fig. 8. Image on the right shows a 3.6 cm thermal emission map of Mercury observed with the VLA. The beam size is 0.4" (1/10 of a Mercurian radius). The direction to the Sun at the time of the observations and the morning terminator (dashed line) are superimposed on the image. The image shows thermal depressions at both poles and along the sunlit side of the morning terminator. Contours are at 42 K intervals except for the lowest contour which is at 8 K (dashed contours are negative). The figure on the right shows the residuals after subtracting a model from the observed map. (from Mitchell and de Pater, 1994).(Mitchell, D.L., and I. de Pater, 1994, Microwave Imaging of Mercury's Thermal Emission: Observations and Models, Icarus, 110, 2-32)

Radio spectra and images, together with Mariner 10 IR data of the planet have been used to infer Mercury's surface properties. At first glance, Mercury's surface is quite similar to that of the Moon. Due to the fact that Mercury, like the Moon, is continuously bombarded by small meteorites, one would expect the top few centimeters to have a very low density, while deeper layers are more compact. Observations indeed show that this is the case on both bodies. Researchers found that the microwave opacity on Mercury is roughly a factor of 2-3 smaller than that of most lunar samples. This suggests that the ilmenite content, which is the most common titanium-bearing mineral on the Moon ((Fe,Mg)TiO), is much less abundant on Mercury than on the Moon. Ilmenite is also opaque at optical wavelengths and is largely responsible for the dark appearance of the moon's maria compared to its highlands. Its absence would explain why Mercury is brighter than the Moon at visible wavelengths.

{7A->7, 7B->8}

B. Venus

Venus has the densest atmosphere of all the terrestrial planets. The principal atmospheric constituents are carbon dioxide and nitrogen (N_2); their mixing ratios are approximately 96.5 % and 3.5% respectively below 100 km altitude. Trace constituents below 100 km altitude are in the range of 0.1 %. The Venus atmosphere is covered with thick clouds composed primarily of sulfuric acid and contaminants, making the surface invisible from above. The total pressure at the bottom of the cloud layer(~47 km) is approximately 1.3 atmospheres. Water is highly depleted throughout the atmosphere. The mean physical structure of the atmosphere (pressure and temperature profile) is reasonably well known from the data returned by a number of space probes. The surface pressure and temperature (on a mean surface) are approximately 94 atm and 737 K, respectively.

The effective temperature of Venus deduced from measurements in the infrared is about 240 ± 8 K, corresponding to an altitude of approximately 60 km. Below this level, the temperature distribution generally follows that for an atmosphere that is in convective equilibrium. Convective equilibrium implies that the temperature gradient in the atmosphere is close to the adiabatic value. The temperature gradient is approximately 8.6 K/km. The high surface temperature is believed to be due to the greenhouse effect. The physical basis for this is that the visible light from the sun is only partially absorbed by the clouds and atmosphere. Some of the light reaches the surface and warms it. The heated surface reradiates in the infrared. The atmosphere is highly absorbing in the infrared spectral region to CO_2 and perhaps H_2O. The atmospheric opacity traps the infrared radiation, thereby raising the surface temperature.

The atmosphere of Venus is opaque at millimeter and short centimeter wavelengths, gradually becoming transparent at longer wavelengths. Individual spectral lines are not observable below the clouds because of pressure broadening. The total vertical optical depth of the atmosphere of Venus at a wavelength of 1 cm is estimated to be slightly less than 20 and to vary approximately as λ^{-2} (optical depth = 1 at ~4 cm). A little more than half of the total opacity is due to collision-induced, non-resonant absorption in CO_2; the remaining opacity is produced by the minor constituents in the atmosphere. Other known or suspected microwave absorbers in the atmosphere are H_2O, SO_2, H_2SO_4, and the sulfuric acid particles in the clouds. Near wavelengths of 6 cm and longward, the atmosphere is sufficiently transparent that it is possible to measure the surface temperature of Venus using radio astronomical methods . The right side of Fig. 8 shows the continuum spectrum of Venus from a few millimeters wavelength out to approximately 6 cm. The left side of Fig. 9 shows the temperature versus altitude profile of Venus. The brightness temperature is seen to rise from about 225 K and 3 mm to about 700 K near 6 cm. This increase in brightness temperature is due to the decreasing opacity of the atmosphere with increasing wavelength. The decreasing opacity allows radio waves to escape from deeper regions in the atmosphere, where it is warmer due to the adiabatic lapse rate. At wavelengths longer than ~15 cm the brightness temperature decreases to ~600 K.

FIG. 9. Schematic representation of the spectrum of Venus from 1 mm to 6 cm (right) and temperature versus altitude profile (left). The figure illustrates how the atmosphere is probed in altitude by changing the wavelengths of the observations.

Radio interferometer data, radar data, and spacecraft data have been used to study the surface of Venus, in particular to determine the dielectric constant. Radar reflectivity data place the dielectric constant in the range 4–5. The Magellan radiometer experiment observed the 12.6-cm-wavelength radio emissivity of more than 91% of the Venus surface. With its 2deg beam width, Magellan observations achieved surface resolutions that varied from 15 by 23 km at periapsis (10degN latitude) to about 85 km at the north pole The global mean value of emissivity seen using horizontal linear polarization is 0.845, a value that corresponds to a dielectric permittivity of between 4.0 and 4.5, depending on the surface roughness. These values are considerably greater than the values for Mercury, Mars, and the moon, which range from 2.0 to 2.5. The higher values are suggestive of a surface composed of dry rock not unlike many rocks of the Earth's surface. These values are consistent with the dry basaltic minerals thought to compose the bulk of the Venus surface. The observations have confirmed earlier findings that a few

regions on Venus, primarily located at high elevations, possess unexpectedly low values of radiothermal emissivity, occasionally reaching as low as 0.3.

Carbon monoxide is an important constituent of the upper atmosphere of Venus. It is formed primarily by the dissociation of carbon dioxide by solar ultraviolet radiation and is removed by chemical and transport processes in the atmosphere. The ground and first excited rotational states of CO (located at very high altitudes in Venus' atmosphere) have been observed to absorb the hot continuous background of the deeper atmosphere. Examples of CO spectra on Venus' day and night side hemisphere are shown in Fig. 10. Observed spectral lines have included ^{12}CO(0-1), ^{12}CO(1-2), C^{18}O(1-2), and ^{13}CO(1-2). These observations have been particularly useful for exploring the altitude range from 70 –110 km.

It has been possible to derive the vertical temperature and mixing ratio profiles of CO in the upper atmosphere of Venus from such observations. As shown in Fig. 9, the spectra reveal considerable variability of CO abundance which varies with solar phase angle. The variability is believed to be the result of large-scale circulation in the upper atmosphere of the planet. Detailed studies of this variability have been undertaken with arrays of telescopes, which operate at millimeter wavelengths. With such arrays the planet can be imaged in the CO-lines, so the CO concentration and temperature profile at all solar phase angles can be measured simultaneously. In addition, through measurements of the Doppler shift of the lines at various locations on Venus' disk, the winds in Venus' mesosphere can be studied. For the CO(0-1) transition, a mean wind speed of 100 m/s in the spectral line forming region produces a Doppler shift of 38 KHz. Such Doppler shifts have been observed at altitudes at least as high as 100 km. Continued observations of these spectral lines will lead to a better understanding of the large-scale circulation in Venus' upper atmosphere.

FIG. 10. Observed absorption spectra of $J = 0 \rightarrow 1$ transition of CO in the atmosphere of Venus. Line center frequency is 115 GHz. [Adapted from P. Schloerb (1985), Proc. ESO-IRAM-ONSALA Workshop on Submillimeter Astronomy.]

C. Mars

Mars moves in an orbit slightly larger than the Earth's, always turning its dayside toward the Earth as it approaches. Earth-based measurements of the night side are impossible and phase angle coverage is greatly restricted. The axis of rotation is tilted from the perpendicular to the plane of its orbit by 25°, about the same as for the Earth. Radio observations of the disk brightness temperature of Mars show it to have a nearly flat spectrum from about 1-mm to 21

cm. The mean disk brightness temperature is about 215 K. As seen from the Earth, the average surface disk temperature varies by ±15 K as the sub-Earth point moves from afternoon to morning and from mid-latitudes to equatorial latitudes. Thus far, most observational data used in thermal modeling studies have come from infrared measurements made from spacecraft. The infrared measurements are limited to the near surface properties. Microwave images obtained with the VLA have extended the thermal models to the subsurface layers of the planet. Microwave images in contrast to single dish observations also yield information on the spatial variations of the brightness temperature. For example, VLA images show the polar regions to be significantly colder than the disk-averaged temperature.

The centimeter radio brightness temperatures of Mars have been found to vary as a function of the central meridian longitude of the planet. Temperature differences as large as 5–10 K are observed over the full range of longitudes. The variations are believed to be due to nonconformity in the Martian surface properties; however, no completely satisfactory explanation of the observations exists.

The Martian atmosphere is very tenuous, having a surface pressure some 200 times less than on the Earth. The primary constituent of the lower atmosphere is CO_2. Photolysis of CO_2 by solar ultraviolet radiation produces CO and O_2. The diatomic molecule CO plays an important role in determining the millimeter wave spectrum of Mars.

Both the ground state and first excited state transitions of CO have been observed in the Martian atmosphere. The altitude distribution of CO has been inferred by interpreting the observed line shape in terms of pressure broadening. A column abundance of CO equal to 2–5 x 10^{20} molecules/cm^2 has been derived from the measurements. This number is very stable over time, even though the CO line profiles show significant variability. This variability has been used to `monitor' Mars's thermal structure: the atmospheric temperature rises significantly during global dust storms, since the dust grains, heated by the Sun, warm up the atmosphere while at the same time preventing sunlight from penetrating down to the surface. Water vapor (from HDO observations at 226 GHz) has also been observed on Mars and used to determine water vapor distribution and atmospheric behaviour. Clancy and collaborators used the VLA at a wavelength near 1.35 cm to image the water vapor in Mars's atmosphere. The water vapor shows up in emission around the planet, where the pathlength through the atmosphere is largest. The data clearly show the absence of emission over Mars' polar caps, where the atmospheric temperature is so low that all the water has been frozen out. We note that the groundbased detection of water vapor in Mars's atmosphere could only be achieved because of the VLA's high angular resolution, so that the atmosphere on the limb could be separated from the planet itself.

D. Jupiter

Jupiter is the first planet detected at radio wavelengths. The discovery observations occurred in 1955, at the very low frequency of 22.2 MHz. Pre-discovery observations of Jupiter were later traced back to 1950. Subsequent observations of Jupiter revealed that its radio spectrum is exceedingly complex, showing both thermal and nonthermal emission mechanisms. Thermal emission from the atmosphere dominates the Jovian spectrum shortward of 7 cm. Nonthermal synchrotron emission dominates the spectrum from ~3 m to 7 cm; brightness temperatures exceed 10^5 K for the synchrotron component. Longward of 7.5 m, Jupiter emits strong and sporadic nonthermal radiation. The radiation exhibits complex frequency, time, and polarization structure. The brightness temperature of this component exceeds 10^{17} K, suggesting a coherent source of emission. The schematic appearance of Jupiter's spectrum is shown in Fig. 11.

FIG. 11. Schematic representation of the spectrum of Jupiter, showing the frequency ranges for which atmospheric emission dominates, synchrotron emission dominates, and sporadic nonthermal emission dominates.

Observations of Jupiter at high angular resolution with radio interferometers have been used to map the synchrotron radiation from Jupiter's radiation belts and to separate the thermal from the nonthermal synchrotron components. The nonthermal component is easily identifiable with a radio interferometer because it is greatly extended relative to the optical disk of Jupiter and is strongly linearly polarized.

The thermal component originates in the Jovian atmosphere. The observations are consistent with a deep model atmosphere, composed mostly of hydrogen and helium, in convective equilibrium. The principal source of opacity is ammonia (NH_3), which exhibits very strong absorption in the microwave spectral region.

In Dec. 1995 the Galileo spacecraft released a probe into the atmosphere of Jupiter, which relayed its findings to the spacecraft via radio signals at a frequency of 1.4 GHz. By analyzing the attenuation of the probe radio signal, the ammonia abundance in Jupiter's deep atmosphere (at pressures over 8 bar) was derived to be a factor of ~3.5 larger than the solar N value. Ground based microwave measurements are most sensitive to layers where the clouds form (~0.5 bar) down to roughly 10-15 bar. The ground based microwave measurements do not show as much ammonia as the probe. Apparently, the ammonia abundance in Jupiter's deep atmosphere is significantly decreased at higher altitudes, to roughly half the solar N value just below the upper

cloud deck. Scientists do not (yet) understand why there is so much less ammonia in the upper regions of Jupiter's atmosphere compared to deeper layers.

VLA images resolve the disk of Jupiter and show the familiar zone-belt structure at 2-6 cm. Figure 12 shows a 1.2 arc second resolution VLA radio image at 2 cm wavelength. The disk diameter of Jupiter was 32 arc sec at the time of the radio observations. Radio images, such as shown in Fig. 12, are usually smeared in longitude, since the observations are integrated over a substantial time interval. The bright (white) belt like regions are indicative of a higher brightness temperature, which is likely due to a relative depletion of NH_3 gas compared to the darker colored regions. Since the radio waves originate in and below the visible cloud layers, such images contain information complementary to that obtained at IR and optical wavelengths. From the images, the latitudinal variation of NH_3 gas can be obtained, in addition to the altitude distribution. Such variations must be due to dynamical processes on the planets, for example, zonal winds, upwelling, and subsidence of gas. The zone-belt structure on Jupiter is consistent with upwelling gas in the zones and subsidence in the belts. Images taken in different years show clear variations in the zone-belt structure, indicative of meteorological changes.

FIG. 12. Radio photograph of Jupiter at a wavelength of 2.0 cm obtained with the VLA. Resolution is 1.2 arc sec. Equatorial diameter of Jupiter is 32 arc sec.

Radio interferometric maps of Jupiter's synchrotron emission have been made at a number of different wavelengths. It has been possible to deduce a great deal of information about Jupiter's magnetosphere from the radio measurements. The radio astronomical measurements provided convincing proof that Jupiter has a strong magnetic field, and this information was used to design the first spacecraft sent to Jupiter. The radio measurements show that the magnetic field is primarily dipolar in shape with the dipole axis tilted about 10° with respect to Jupiter's rotational axis. Using the well-developed theory of synchrotron emission (summarized in Section II-C), it has been possible to determine energies and densities of the high-energy electrons that are trapped in Jupiter's magnetic field.

Fig 13 shows a radio image of Jupiter's synchrotron radiation. The main radiation peaks are indicated by the letters L and R, and the high latitude emission peaks by Ln, Ls, Rn and Rs. Magnetic field lines at jovicentric distances of 1.5 and 2.5 (from the O6 magnetic field model) are superimposed. The resolution is 0.3 Jovian radii, roughly the size of the high latitude emission regions. Thermal emission from Jupiter's atmosphere appears as a disk shaped region in the center of the figure

Fig. 13. Radio photograph of Jupiter's synchrotron emission at a jovicentric longitude of 312°. The image was taken at a wavelength of 20 cm, using the Very Large Array in June, 1994 (de Pater and Sault, 1998, J. Geophys. Res. Planets, 103, No. E9, 19,973-19, 984)

Fig. 14 shows a tomographic map of the emission region, obtained by observing Jupiter at all longitudes and reconstructing a 3 dimensional map. The emission is seen to be confined to the magnetic equatorial plane out to a distance of ~ 4 Jovian radii. Several intriguing features are visible. The main radiation peaks (L and R on Fig. 13) are usually asymmetric. One of the peaks appears to be brighter than the other peak. The asymmetry of these main radiation peaks is caused by deviations in Jupiter's magnetic field from a pure dipole configuration. These deviations are evident in Fig. 14, where the main ring of radiation is clearly warped like the surface of a potato chip. If Jupiter's field were a dipole field, this ring would be flat, and the radiation peaks (Fig. 13) would always be equal in intensity, though the intensity would vary with jovian rotation, such that it would be smallest when one of the magnetic poles is directed towards us. The secondary emission peaks (Ln, Ls, Rs, Rn in Fig. 13) become high latitude rings when viewed in a three-dimensional image. These peaks are produced by electrons at their mirror points, and they reveal the presence of a relatively large number of electrons which bounce up and down the field lines at a Jovian distance of 2 --2.5 Jovian radii. It is believed that these electrons may have been scattered out of the magnetic equatorial plane, perhaps by the moon Amalthea which orbits Jupiter at a distance of 2.5 Jovian radii.

Fig. 14: Three-dimensional tomographic reconstruction of Jupiter's nonthermal radio emissivity. The planet itself is shown as a black sphere in this visualization. (de Pater and Sault, 1998,J. Geophys. Res. Planets, 103, No. E9, 19,973-19, 984).

The total radio intensity of Jupiter varies significantly over time (years), and appears to be correlated with solar wind parameters. The impact of comet D/Shoemaker-Levy 9 with Jupiter in July 1994 caused a sudden sharp increase in Jupiter's total flux density, by ~ 20%. At the same time the brightness distribution of the radio flux density changed drastically. These observations

suggest that the impact and associated phenomena significantly modified the electron distribution and possibly the magnetic field as well.

At frequencies below 40 MHz, Jupiter is a strong emitter of sporadic nonthermal radiation. A decameter wavelength (DAM) component observable from the ground is characterized by complex, highly organized structure in the frequency-time domain and dependent on the observer's position relative to Jupiter. The satellite Io modulates the DAM emission. The Voyager spacecraft added significantly to our knowledge of this low-frequency component when it flew by Jupiter in 1979. A kilometric wavelength (KOM)component was discovered at frequencies below 1 MHz and the observations of the DAM component were significantly improved. The extremely high brightness temperatures ($>10^{17}$ K), narrow-bandwidth emissions, and sporadic nature all suggest that the very low frequency emissions from Jupiter are generated by energetic particles acting coherently and interacting with the plasma that surrounds Jupiter. The details of the emission process are not well understood at present.

E. Saturn

Radio emission from Saturn has been observed from the Earth over a wavelength range from 1 mm to approximately 70-cm. The emission is thermal throughout this band, arising in both the atmosphere and the rings. The atmospheric emission is similar to that observed from Jupiter. Model studies indicate that Saturn, like Jupiter, has a deep convective atmosphere. Hydrogen and helium form the bulk of the atmosphere, whereas ammonia in trace amounts provides most of the microwave opacity. High-resolution radio images of Saturn also give information on the latitudinal distribution of NH_3 gas. Figure 15 shows a VLA image at 6-cm wavelength: the resolution is 1.5 arc sec and disk diameter 16.8 arc sec. A bright band can be distinguished at mid-latitudes, indicative of an average lack of NH_3 gas over the altitude region probed at this wavelength. The region at mid-latitudes is likely a region of subsiding gas, just like the bright belts seen on Jupiter. In the nineties the zonal patterns on Saturn changed drastically compared to what was seen in the eighties, indicative of strong dynamical interactions.

As shown in Figures 15 and 16, interferometer observations of Saturn also detect the thermal emission from the ring particles. Most of the radio emission is due to scattering of Saturn's emission off the ring particles. In front of the planet, the rings are visible as an absorption feature; they block out Saturn's radio emission. The scattering characteristics of the rings contain information on the ring particle sizes and composition.

FIG. 15. Radio photograph of Saturn at a wavelength of 6.14 cm obtained with the VLA. Resolution is 1.5 arcsec. Equatorial diameter of Saturn is 16.83 arc sec. (de Pater, I., and J.R. Dickel, 1991, Icarus **94**, 474-492)

FIG. 16. Radio photograph of Saturn at a wavelength of 2.0 cm obtained with the VLA. Resolution is 1.5 arc sec. Equatorial diameter of Saturn is16.83 arc sec.. (de Pater, I., and J.R. Dickel, 1991, Icarus **94**, 474-492)

Interferometer observations of Saturn at centimeter and millimeter wavelengths have detected thermal emission from the ring particles. The rings have a low brightness temperature, approximately 10 K. The presence of ring particle sizes larger than a few centimeters are suggested by the radio observations. The observations are consistent with the bulk properties of the ring particles being those of water ice.

The Voyager spacecraft detected two distinct classes of nonthermal emissions from Saturn at frequencies below 1 MHz. These emissions are not observable from the Earth because of the opaqueness of the Earth's ionosphere at frequencies below a few megacycles. The first class, called Saturn kilometric radiation, is a relatively narrow band polarized emission. The second class is a broadband, impulsive emission called Saturn electrostatic discharge.

F. Uranus

Uranus is unique among the planets in having its rotation axis tilted close to the plane of the ecliptic. The north pole of Uranus is inclined ~98° to the ecliptic plane (8° south of the plane), and the seasons on Uranus average 21 terrestrial years in length. The effect of this geometry on the large-scale circulation of the Uranium atmosphere is not yet fully understood, but it is expected to be significant.

As in the case of both Jupiter and Saturn, the disk brightness temperatures of Uranus significantly exceed the expected equilibrium temperature. The observed temperatures are greater than 100 K at wavelengths greater than a few millimeters and longward, whereas the predicted effective temperature is only about 55 K. The radio emission from Uranus is

unpolarized within the measurement uncertainties of a few percent. Interferometer observations of Uranus show the emission to be confined to the solid angle of the visible disk, providing evidence that the excess emission is from the atmosphere and is not synchrotron emission. It is believed that the emission from Uranus is thermal, originating in the atmosphere of the planet.

The radio emissions from Uranus arise from sufficient depths that collision-induced absorption by hydrogen is an important source of opacity at millimeter wavelengths. Ammonia is severely depleted in Uranus's atmosphere, at least at pressure levels less than 25 bar. Since, based upon planet formation theories, nitrogen must be present in at least solar proportions, it is believed that ammonia gas is abundant at deeper levels, but reacts with H_2S to form a cloud of NH_4SH. If indeed this process accounts for the `observed' depletion in NH_3, hydrogen sulfide should be enriched in Uranus's atmosphere by about an order of magnitude over solar S. Such an abundance of H_2S itself will contribute to the radio opacity in Uranus's atmosphere, and actually help reconcile observed spectra with models.

Another interesting aspect of the radio emission from Uranus is that its total intensity varies slowly over time. With the help of interferometric (VLA) observations, it is well established by now that the Uranus pole is warmer than its equator. This will certainly lead to time variations during Uranus' orbit around the sun. It is not known, however, whether this indeed fully explains the observed time variability.

The Voyager spacecraft detected a wide variety of radio emissions from Uranus during its encounter in January 1986. Most of the emissions were polarized and probably due to maser-cyclotron emission. The emissions range in frequency from about 20 kHz to 800 kHz, well below the frequency range that is observable from the Earth. The emissions suggest a magnetosphere rich in magneto-hydrodynamic phenomena.

G. Neptune

Disk brightness temperature measurements of Neptune at centimeter and millimeter wavelengths are sparse, but existing measurements suggest a spectrum very similar to that of Uranus. The disk brightness temperatures exceed the predicted equilibrium temperature by 50 K or more. High angular resolution measurements obtained with the VLA show that the excess emission is not due to synchrotron emission. As in the case of Uranus, model studies suggest that ammonia must be depleted on Neptune (as on Uranus) by roughly two orders of magnitude compared to solar nitrogen values to explain the high brightness temperatures that are observed.

This depletion may be caused by a nearly complete removal of NH_3 gas in the upper atmosphere through the formation of NH_4SH, the same process which depletes ammonia in the Uranus atmosphere. On Neptune the H_2S abundance must be even larger than on Uranus, about

30 times the solar sulfur/hydrogen ratio. Although ammonia gas may be close to the solar N value in Uranus deep atmosphere, it must be substantial subsolar throughout Neptune. Here a problem arises: A subsolar value for nitrogen gas is inconsistent with theories on planet formation. If a planet forms directly from the primordial solar nebula, the elemental abundances must be equal to that measured on the Sun. Condensable materials accrete as solids, sublime in the protoplanet's atmosphere and therefore enhance the elemental abundances above solar values. Carbon, sulfur and oxygen compounds, present as CH_4, H_2S, and H_2O in the giant planets, are therefore enhanced above solar values. Similarly, nitrogen is expected to be enhanced above solar N. A subsolar value on Neptune is simply not possible. This dilemma got solved, however, with the detection of emission lines in the 1-3 mm band of CO and HCN in Neptune's upper atmosphere.

Since both lines are seen in emission, CO and HCN must be located above the tropopause, in Neptune's stratosphere. Although CO may be brought up from deep depths through rapid convection, HCN must be formed in the stratosphere from nitrogen and carbon products, since HCN, if it would exist in Neptune's deep atmosphere, would freeze out on its way up, well before it could reach the stratosphere. If, however, much of the nitrogen in Neptune's atmosphere would be present in the form of N_2 rather than NH_3, the N_2 might convect rapidly upwards and form HCN in the stratosphere through chemical reactions with carbon products. Moreover, if nitrogen would exist in the form of N_2 rather than NH_3, the total nitrogen abundance in Neptune's atmosphere would be consistent with planet formation theories.

The Voyager spacecraft detected a variety of low frequency radio emissions from Neptune during its encounter in 1989. The emissions were similar to those observed from the other major planets.

H. Comets

Prior to the 1960's, comets were investigated primarily using visible wavelengths observations. The first infrared detection of a comet was achieved in the mid-sixties. Although radio astronomers had attempted to detect cometary emissions since the 1950's, the first widely accepted radio detection of a comet is that of the 18-cm OH transitions in Comet Kohoutek (1973). Radio observations of comets have been used to study all of the major components of comets – nucleus, dust, neutral gas and the plasma.

Continuum observations of thermal emission from comets provides information on the nucleus temperature and on the large dust grains which surround the nucleus. The thermal emission from comets is very weak, and sensitive receiving systems are needed to make a detection. Short centimeter, millimeter, and submillimeter observations have been the most

successful for the detection of thermal emission. In the nineties sensitive detectors at millimeter and submillimeter wavelengths came on line, just in time to observe two very bright comets: comet Hyakutake in 1996 and comet Hale-Bopp in 1997. Radio spectra at submillimeter-millimeter wavelengths were obtained for both comets. The thermal emission is clearly dominated by emission from dust grains, rather than the cometary nucleus, and the data have been used to derive the dust mass and dust mass production rate for each comet. Continuum observations of comets will be greatly improved when the new large millimeter and submillimeter arrays become available and when thermal emission measurements from spacecraft are possible.

Radio astronomy of comets has made its most significant advances in the area of spectroscopy. Many so called 'parent' molecules (molecules which sublimate directly off the nucleus, in contrast to 'daughter' molecules which are products of the parents) have been observed at radio wavelengths through their rotation lines in the millimeter and submillimeter bands. Observations of these spectral lines give valuable information on the icy composition of the cometary nucleus, gas production rates, physical conditions in coma, and on the variation of these in time and heliocentric distance.

The timely appearance of the bright comets Hyakutake and Hale-Bopp greatly expanded our knowledge of cometary volatiles. The number of identified parent molecules increased by more than a factor of two through observations of these comets; most of these new species were detected in the millimeter and submillimeter. Spectroscopic observations of comet Hale-Bopp, which could be followed in its orbit for several years, yielded invaluable data on composition and gas production rates. Gas production rates of different molecules could be followed over large heliocentric distances (Fig. 17). At distances greater than 3 AU, the sublimation was dominated by gases more volatile than water. Carbon monoxide, the most volatile species observed, could be detected at a heliocentric distance of 7 AU. It displayed a steady increase in brightness while the comet moved in towards the Sun. This gas clearly must have been key to the observed visible brightness of the comet at these large heliocentric distances. At a heliocentric distance of 3 AU, OH became the most abundant species, confirming that the composition of the comet is dominated by water-ice (H_2O -> OH + H). Inside a heliocentric distance of 1.5 AU all species showed a dramatic increase in production rates. Radio images of various species have been obtained and have been used to derive the relative importance of sublimation directly from the nucleus or from grains in the coma. This varies from gas to gas, and probably differs from comet to comet.

FIG. 17. Evolution of molecular production rates of comet Hale-Bopp as a function of heliocentric distance. *Left*, preperihelion

data; *Right*, postperihelion data. (Biver, N., Bockelée-Morvan, D., Colom, P., Crovisier, J., Germain, B., Lellouch, E., Davies, J.K., Dent, W.R.F., Moreno, R., Paubert, G., Wink, J., Despois, D., Lis, D.C., Mehringer, D., Benford, D., Gardner, M., Phillips, T.G., Gunnarsson, M., Rickman, H., Bergman, P., Johansson, L.E.B., Winnberg, A., Rauer, H., 1999, Earth, Moon, and Planets, **78**:5-11).

As mentioned above, the first radio detection of a comet was that of the 18-cm OH line. The study of this line has been an important component of cometary research for over twenty five years. The 18-cm line is split into four transitions at 1612, 1665, 1667, and 1721 Mhz. The observed intensity of the OH line is quite variable. The line is seen in emission or absorption depending on the comet's heliocentric velocity. The explanation of this effect is that it is due to pumping of the OH molecules by solar UV photons. If the comet's heliocentric velocity is such that Fraunhofer absorption lines from the Sun shift into the excitation frequency, the OH molecules are not excited. At all other times they are. This variation in excitation is known as the Swings effect. When OH is not excited, it is seen in absorption against the galacticbackground. If it is excited, the emission is actually maser emission rather than simple thermal emission.

V. PROSPECTS FOR THE FUTURE

Planetary radio astronomical observations were initially limited to measurements of the disk-averaged brightness temperatures and to the strong non-thermal radio emission from Jupiter. With improved spatial resolution and high sensitivity receiving systems, it has been possible to map the planets (satellites and comets) and carry out high resolution spectroscopic observations. With the rapidly improving instrumentation now on the horizon, eventually it should be possible to study the planets using ground based and spacecraft instruments in nearly the same detail in which the Earth is being studied with combined sensors on weather satellites and ground stations. As angular resolution improves with time, it should be possible to map the vertical and horizontal distribution of certain chemical species within planetary atmospheres, to measure wind speeds, and to search for local variations in subsurface properties. Both ground-based radio telescopes and spacecraft radio receivers will play a role in future observations. Large ground based telescopes will have sufficient resolution to examine the global properties of the planets out to Neptune and to study satellites, asteroids and comets. The advent of lighter-weight and

lower-power radio receivers will enhance the possibilities of placing radio experiments on spacecraft. Radio telescopes working at submillimeter wavelengths are gradually becoming a reality as a few mountaintop observatories are nearing completion and plans for a submillimeter space telescope are being discussed in a number of countries. The shorter-wavelength region of the spectrum will provide new opportunities to study the upper atmospheres of the planets with spectroscopic techniques capable of detecting heretofore unobserved transitions that occur in the submillimeter and infrared. In addition, the shorter wavelengths will provide high angular resolution with only moderate-size telescopes. In summary, the future prospects for planetary radio astronomy are bright. This optimistic outlook is based on radio astronomical systems currently under development. The evolution of radio technology will undoubtedly lead to an even brighter future for planetary radio astronomy.

Bibliography

Berge, G.L., and Gulkis, S. (1976), Earth-based radio observations of Jupiter: Millimeter to meter wavelengths. *In* "Jupiter" (T. Gehrels, ed.), University of Arizona Pres,s Tuscon.

de Pater, I., 1999, The Solar System at Radio Wavelengths, in the Encyclopedia of the Solar System, eds. P. Weissman, L. McFadden, and T.V. Johnson. Academic Press, Inc., 735-772

de Pater, I. (1990). Radio images of the planets. *Ann. Rev. Astron. Astrophs.* **28,** 347–399.

Dessler, A.J. (Ed.) (1983), "Physics of the Jovian Magnetosphere." University Press, Cambridge, U.K.

Janssen, M. A.(Ed.) (1993). "Atmospheric Remote Sensing By Microwave Radiometry." John Wiley & Sons, Inc.

Lewis, J.S., and Prinn, R.G. (1984). "Planets and Their Atmospheres." Academic Press, Orlando, Florida.

Morrison, D. (1970). Thermophysics of the planet Mercury. *Space Sci. Rev.* **11,** 271–307.

Muhleman, D.O., Orton, G.S., and Berge, G.L. (1979). A model of the Venus atmosphere from radio, radar, and occultation observations. *Astrophys. J.* **234,** 733–745.

Sullivan, W.T., III (Ed.) (1984). "The Early Years of Radio Astronomy." University Press, Cambridge, U.K.

Fig 1

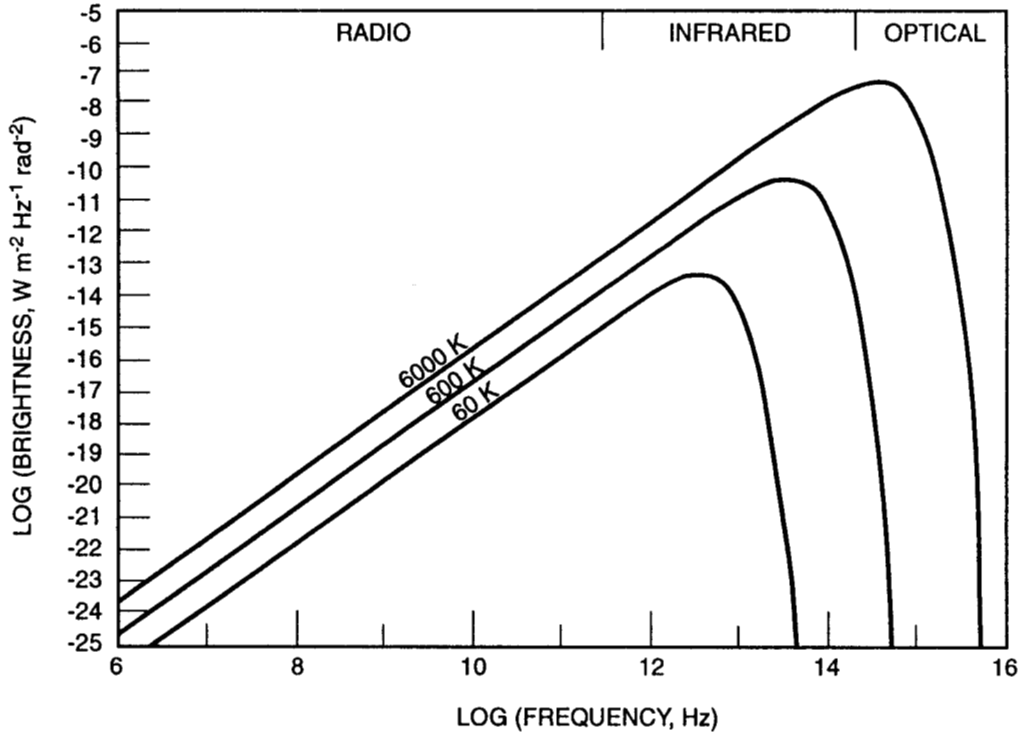
RADIO
INFRARED
OPTICAL
6000 K
600 K
60 K
LOG (BRIGHTNESS, W m-2 Hz-1 rad-2)
-5
-6
-7
-8
-9
-10
-11
-12
-13
-14
-15
-16
-17
-18
-19
-20
-21
-22
-23
-24
-25
6
8
10
12
14
16
LOG (FREQUENCY, Hz)

Fig 2

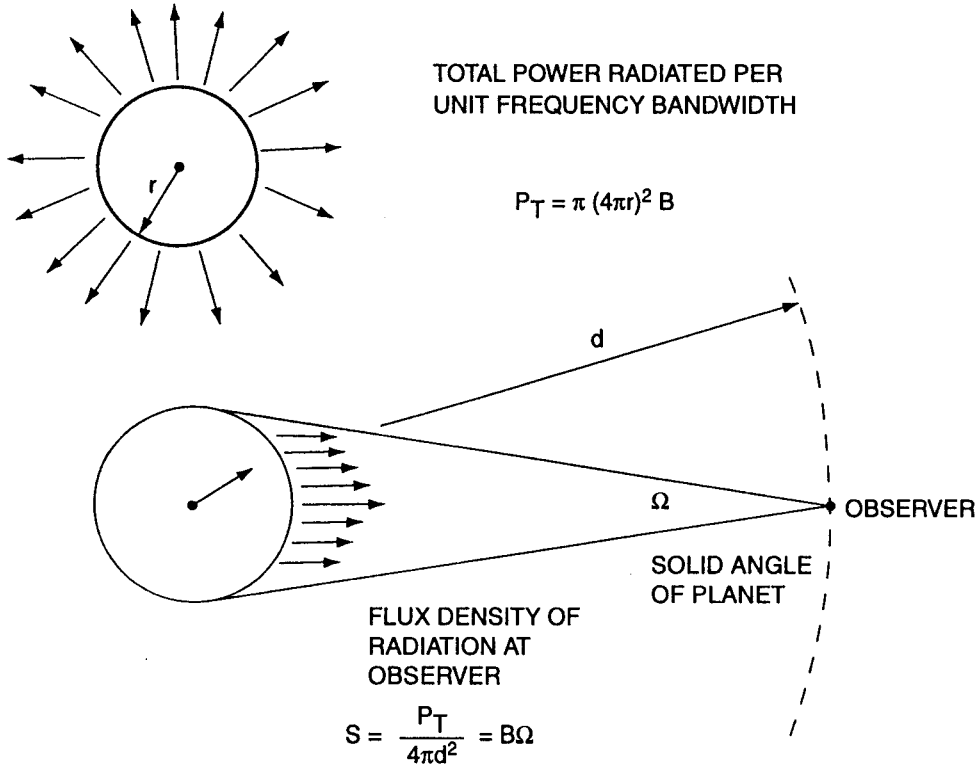
r
TOTAL POWER RADIATED PER
UNIT FREQUENCY BANDWIDTH
$P_T = \pi (4\pi r)^2 B$
d
Ω
OBSERVER
SOLID ANGLE
OF PLANET
FLUX DENSITY OF
RADIATION AT
OBSERVER
$S = \frac{P_T}{4\pi d^2} = B\Omega$

Fig 3

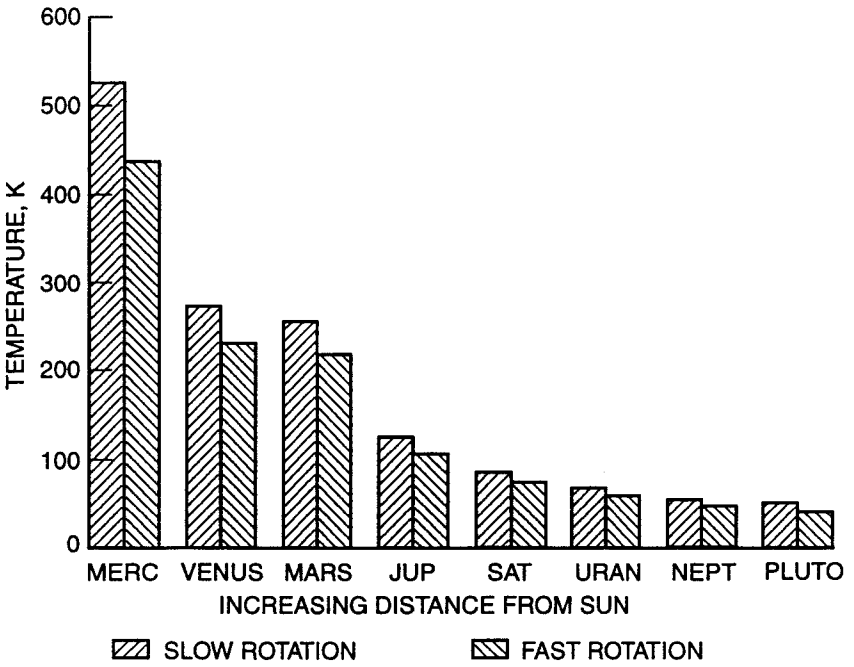
600
500
400
300
200
100
0
TEMPERATURE, K
MERC
VENUS
MARS
JUP
SAT
URAN
NEPT
PLUTO
INCREASING DISTANCE FROM SUN
SLOW ROTATION
FAST ROTATION

Fig 4

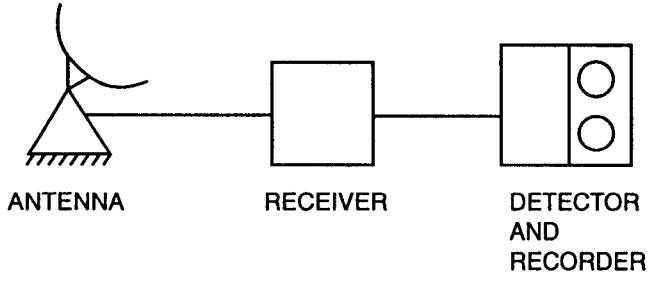

Fig 5

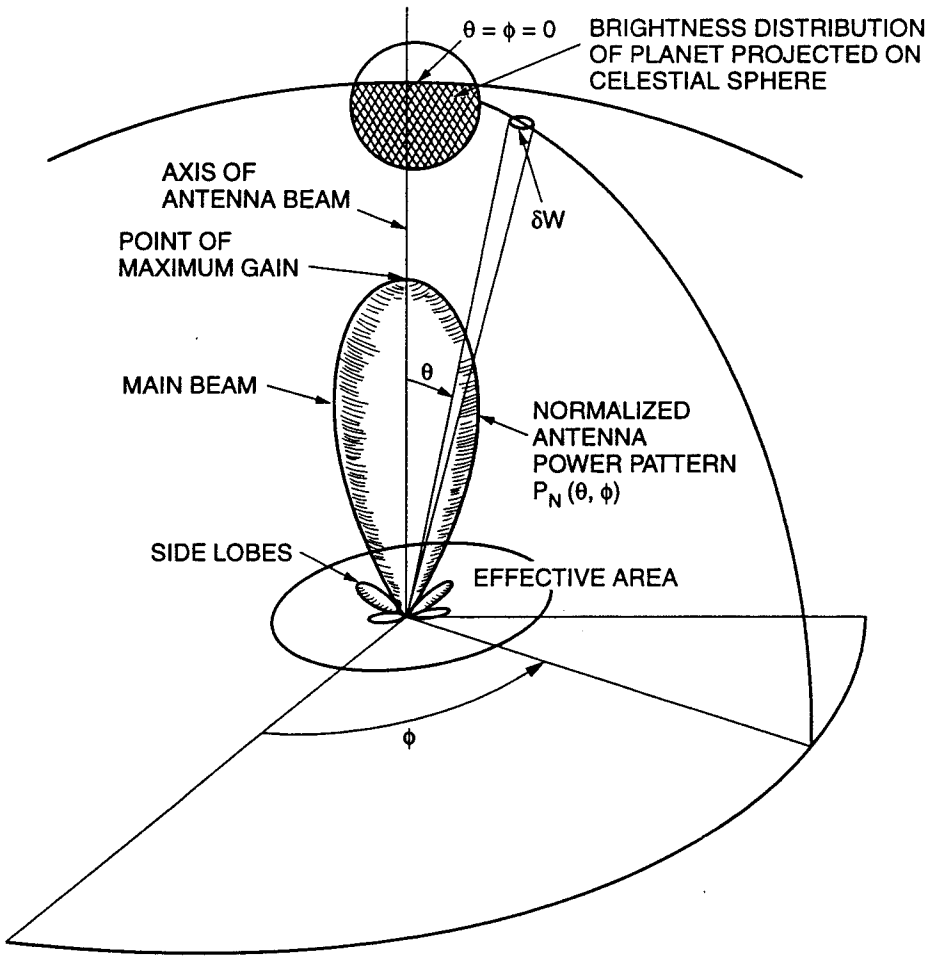
θ = ϕ = 0
BRIGHTNESS DISTRIBUTION OF PLANET PROJECTED ON CELESTIAL SPHERE
AXIS OF ANTENNA BEAM
δW
POINT OF MAXIMUM GAIN
MAIN BEAM
θ
NORMALIZED ANTENNA POWER PATTERN
$P_N(\theta, \phi)$
SIDE LOBES
EFFECTIVE AREA
ϕ

Fig 6

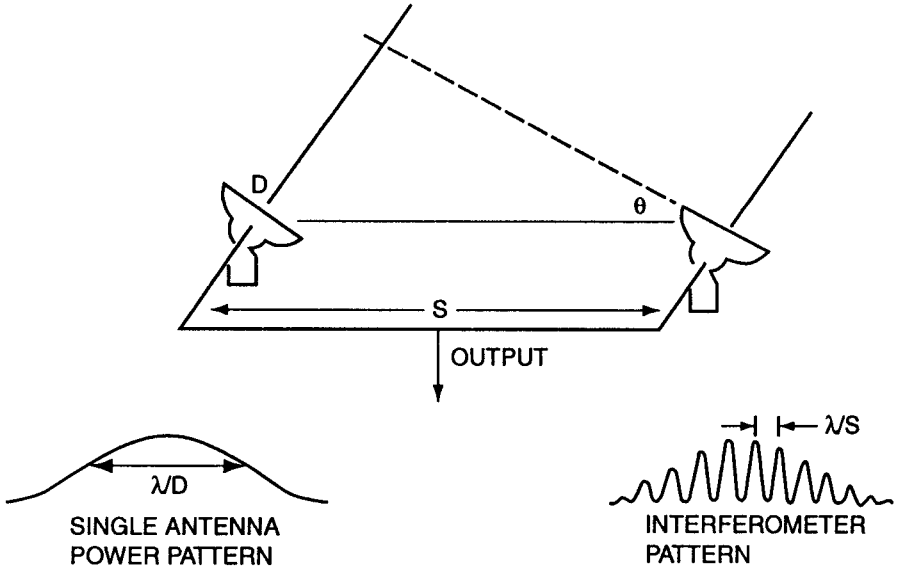
D
θ
S
OUTPUT
λ/D
SINGLE ANTENNA
POWER PATTERN
λ/S
INTERFEROMETER
PATTERN

Fig 7

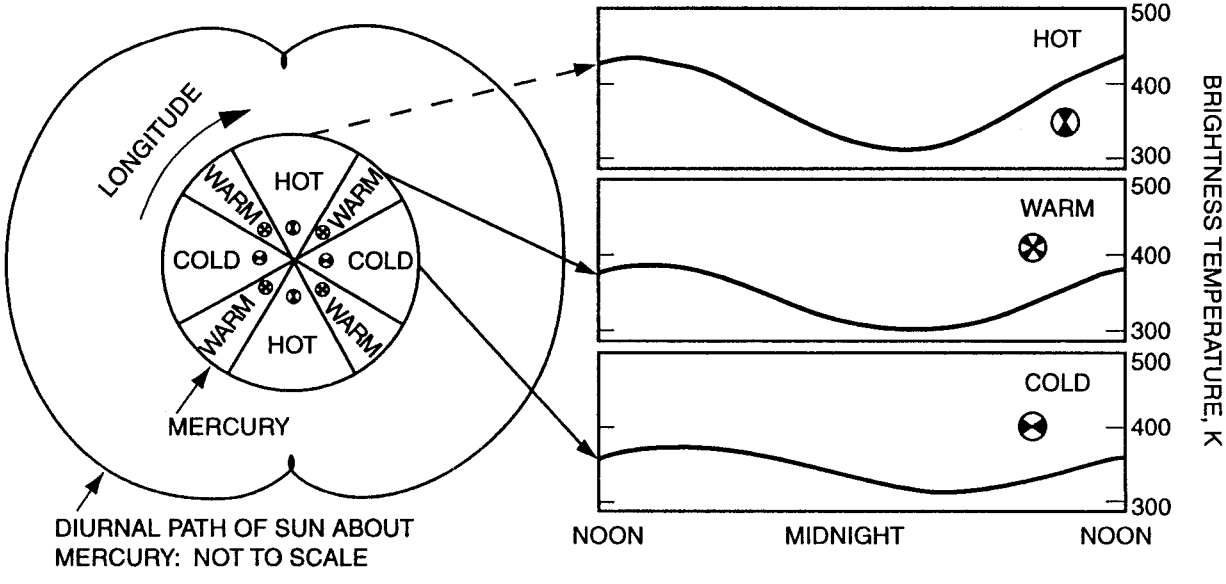
LONGITUDE
HOT
WARM
WARM
COLD
COLD
WARM
WARM
HOT
MERCURY
DIURNAL PATH OF SUN ABOUT
MERCURY: NOT TO SCALE
HOT
WARM
COLD
500
400
300
BRIGHTNESS TEMPERATURE, K
NOON
MIDNIGHT
NOON

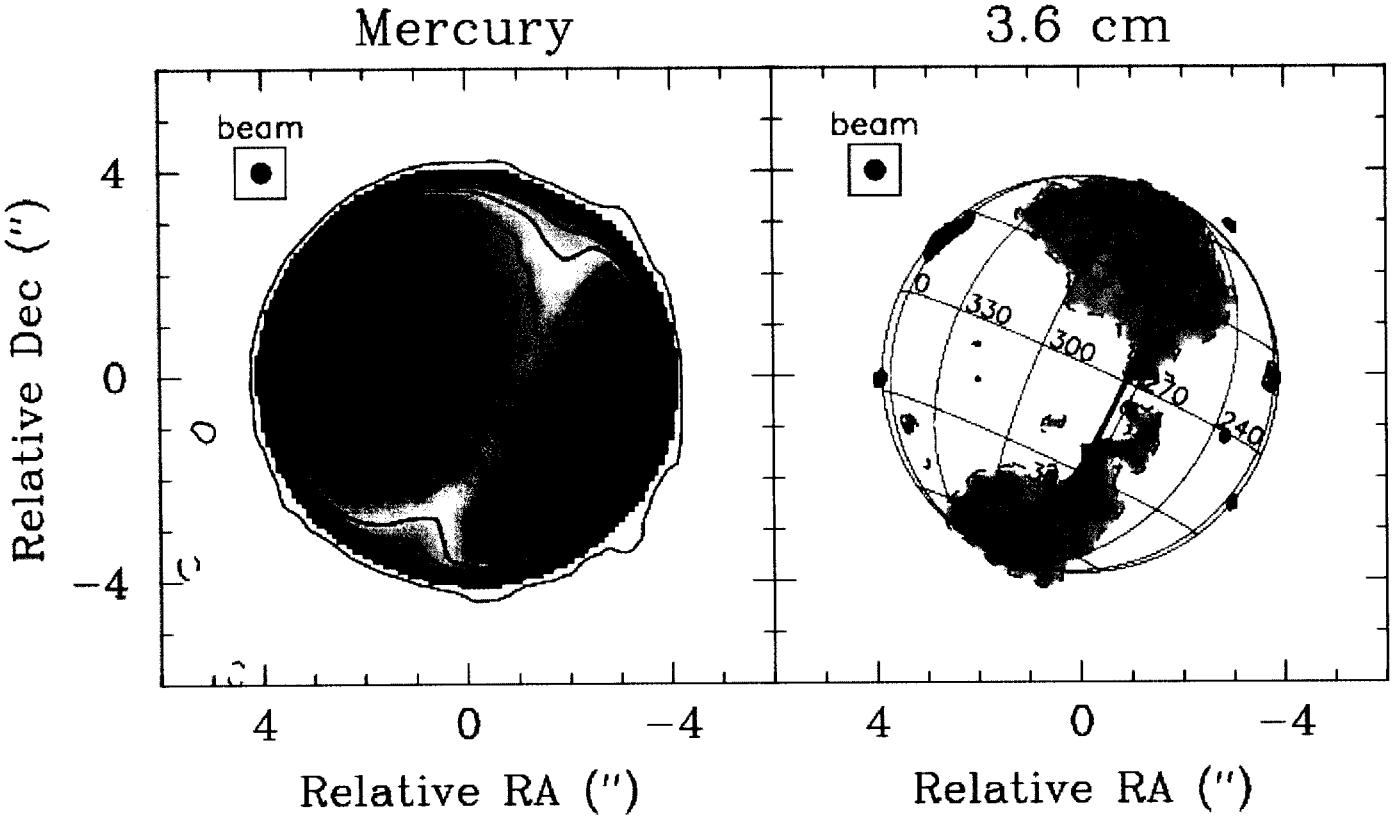
Mercury
3.6 cm
beam
beam
Relative Dec (")
4
0
−4
4
0
−4
Relative RA (")
Relative RA (")
0
330
300
270
240

Fig 8.eps

Fig 9

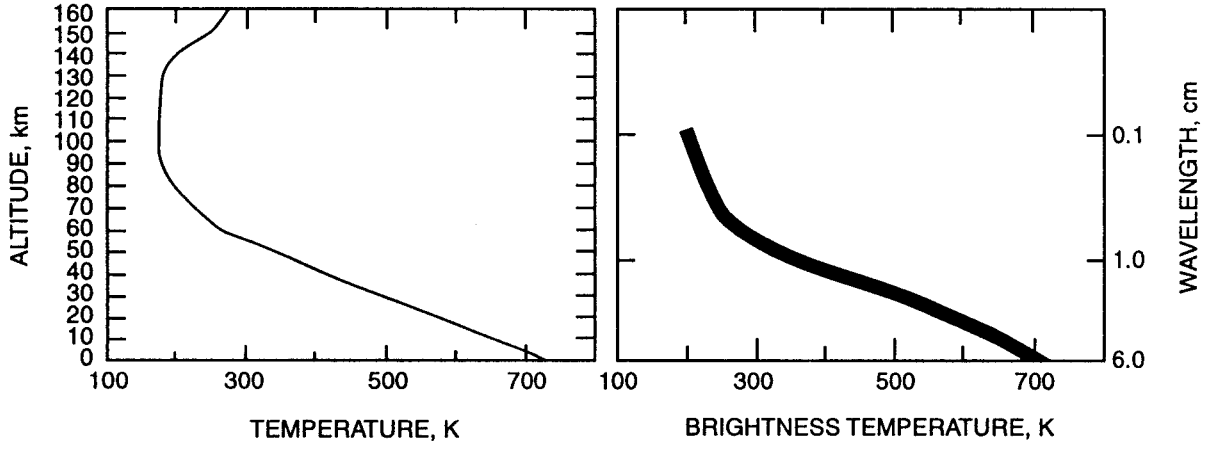
ALTITUDE, km
160
150
140
130
120
110
100
90
80
70
60
50
40
30
20
10
0
100
300
500
700
TEMPERATURE, K
100
300
500
700
BRIGHTNESS TEMPERATURE, K
0.1
1.0
6.0
WAVELENGTH, cm

Fig 10

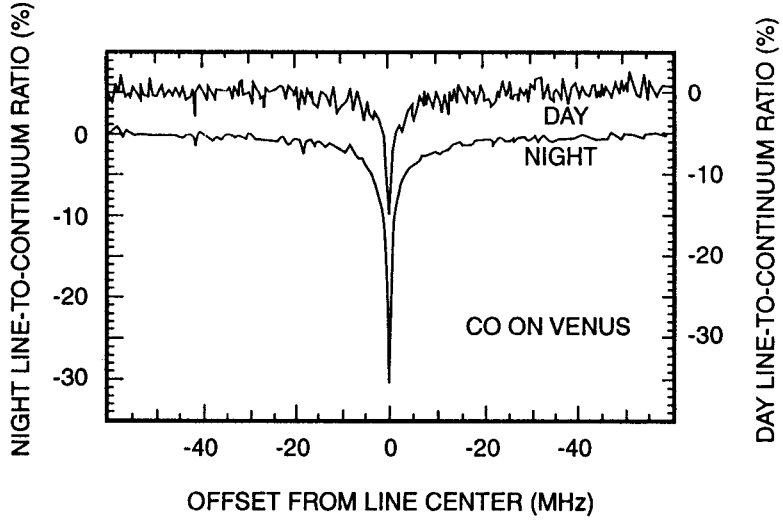
NIGHT LINE-TO-CONTINUUM RATIO (%)
DAY LINE-TO-CONTINUUM RATIO (%)
0
-10
-20
-30
DAY
NIGHT
CO ON VENUS
-40
-20
0
-20
-40
OFFSET FROM LINE CENTER (MHz)

Fig 11

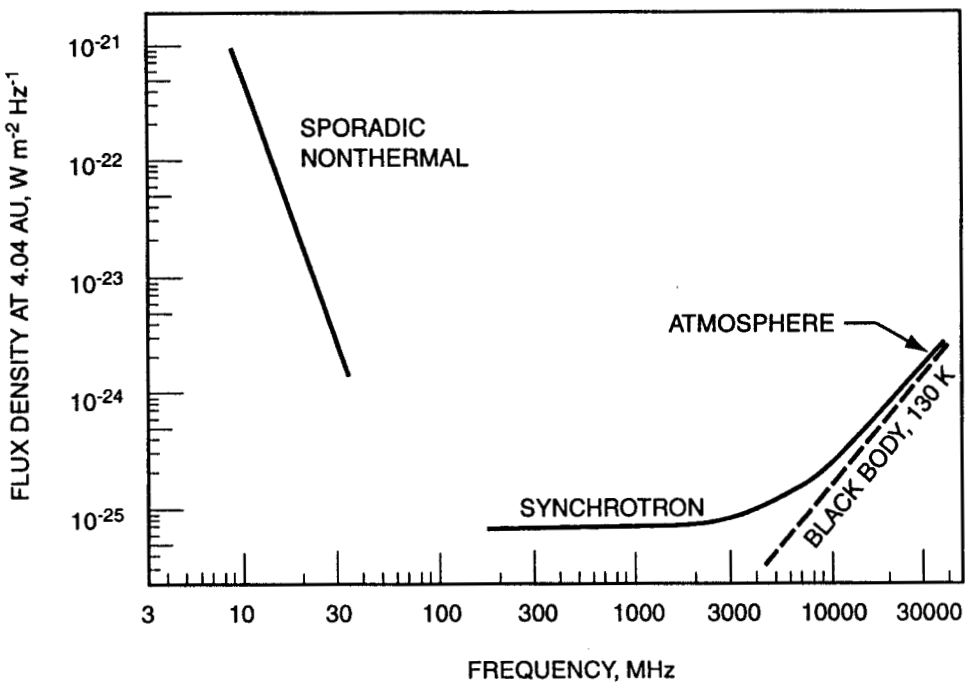
FLUX DENSITY AT 4.04 AU, W m^{-2} Hz^{-1}
10^{-21}
10^{-22}
10^{-23}
10^{-24}
10^{-25}
SPORADIC
NONTHERMAL
ATMOSPHERE
BLACK BODY, 130 K
SYNCHROTRON
3
10
30
100
300
1000
3000
10000
30000
FREQUENCY, MHz

Fig 12

Fig 13

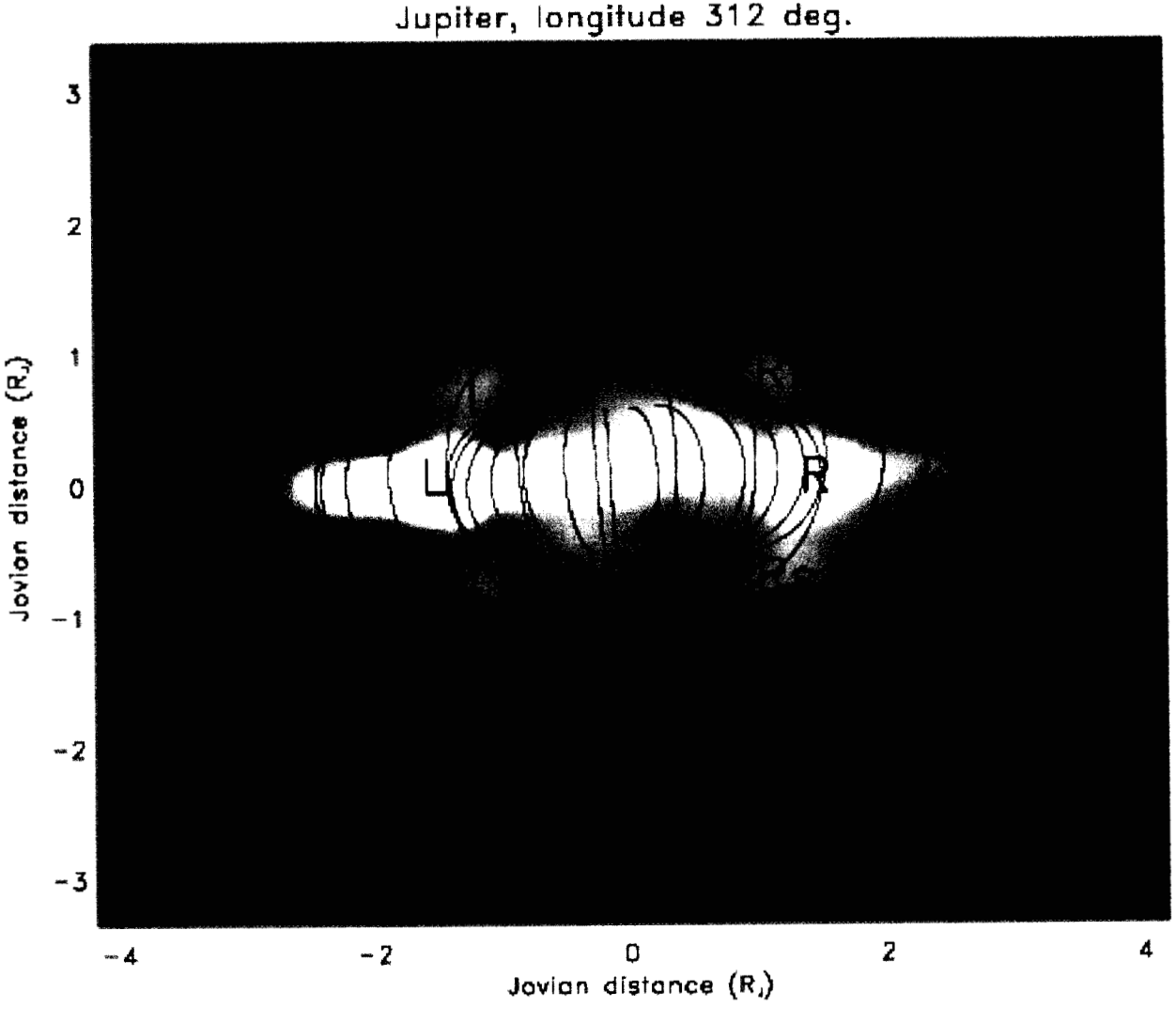
Jupiter, longitude 312 deg.
Jovian distance (R_J)
3
2
1
0
−1
−2
−3
L
R
−4
−2
0
2
4
Jovian distance (R_J)

Fig 14

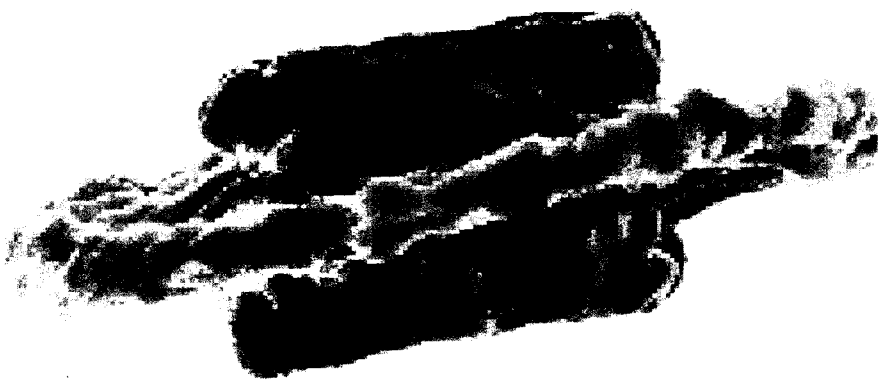

Fig 15

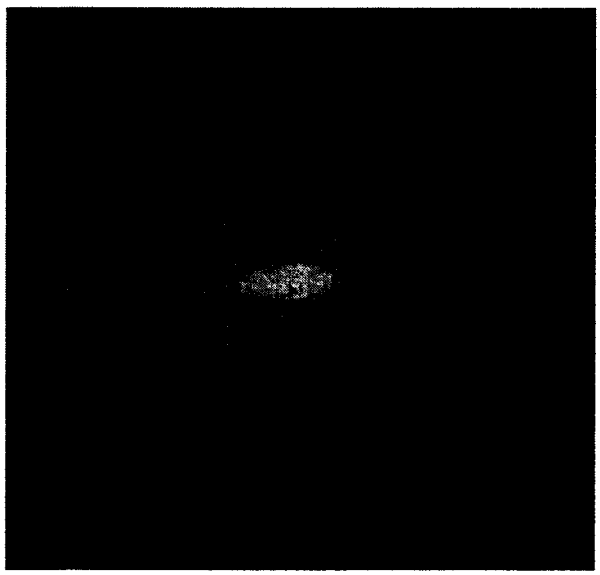

Fig 16

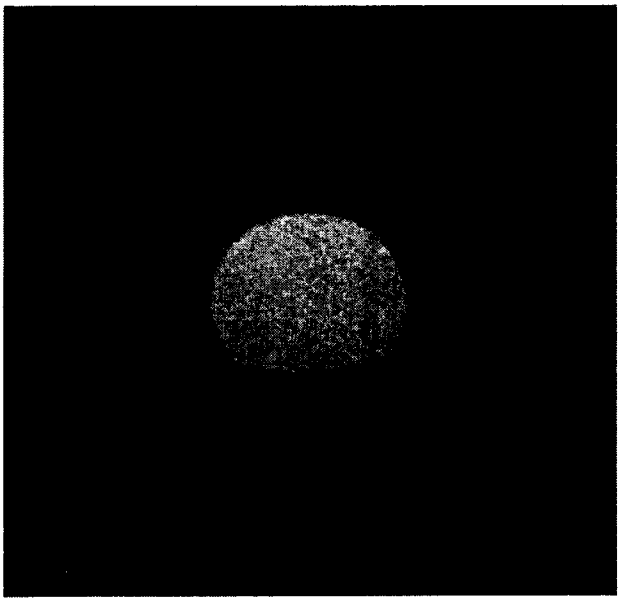

Fig 17

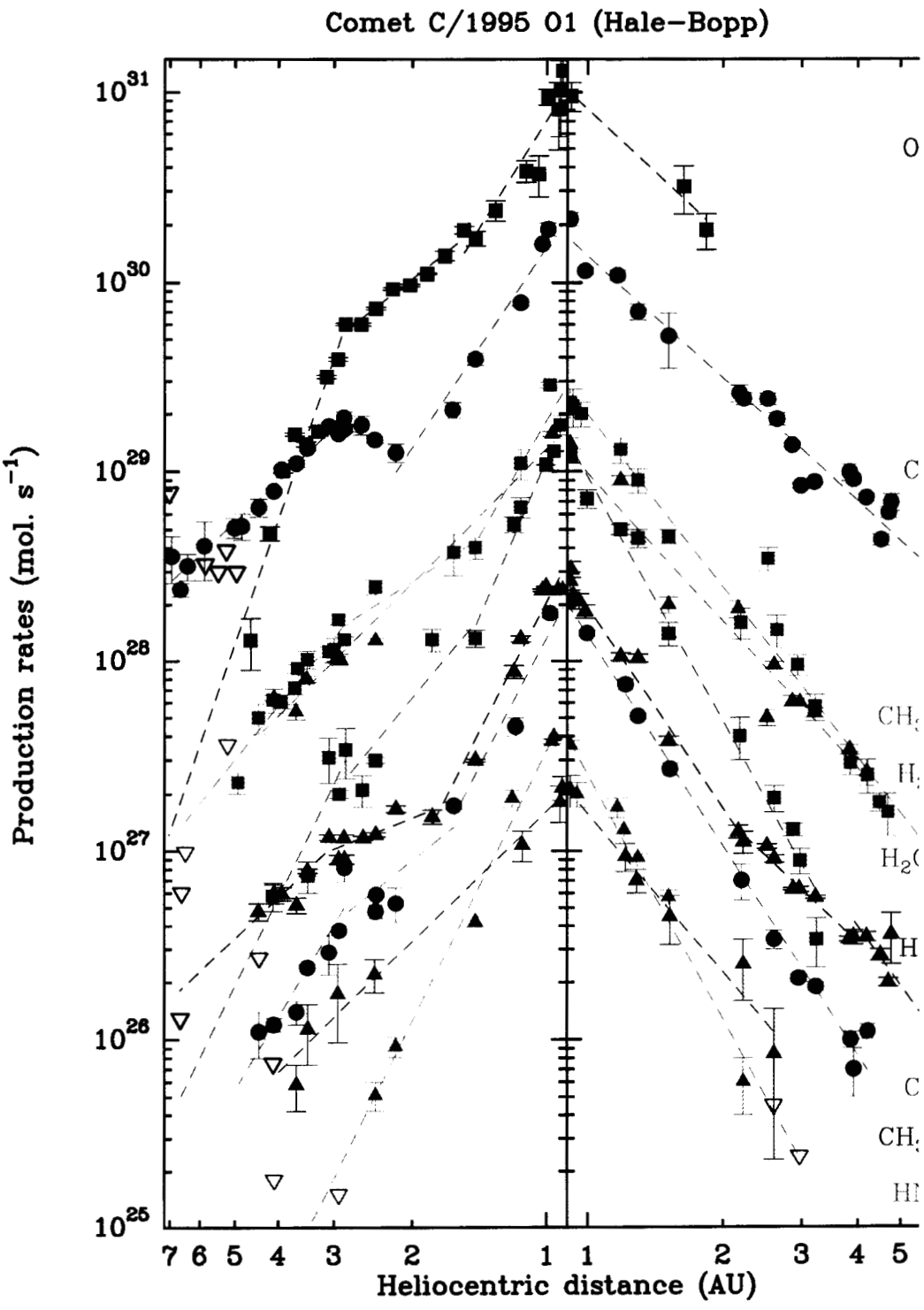
Comet C/1995 O1 (Hale–Bopp)
Production rates (mol. s^{-1})
10^{31}
10^{30}
10^{29}
10^{28}
10^{27}
10^{26}
10^{25}
O
C
CH_3
H_2
H_2C
H
C
CH_3
HI
7 6 5 4 3 2 1 1 2 3 4 5
Heliocentric distance (AU)